



Article

Productivity Model Study of Water-Bearing Tight Gas Reservoirs Considering Micro- to Nano-Scale Effects

Feifei Chen ^{1,*}, Yonggang Duan ¹ and Kun Wang ²

¹ State Key Laboratory of Oil and Gas Reservoir Geology and Exploitation, Southwest Petroleum University, Chengdu 610500, China; nanchongdyg@163.com

² Nanhai East Petroleum Research Institute, Shenzhen Branch of CNOOC Limited, Shenzhen 518000, China; wangkun25@cnooc.com.cn

* Correspondence: cff1004@163.com

Abstract: Tight sandstone is rich in micron- and nano-scale pores, making the two-phase flow of gas and water complex. Establishing reliable relative permeability and productivity models is an urgent issue. In this study, we first used a slip model to correct the gas phase's no-slip Hagen–Poiseuille equation for nano- and micropores. Then, combined with the fractal theory of porous media and the tortuous capillary bundle model, we established two-phase relative permeability models for nanopores and micropores. These relative permeability models comprehensively consider the gas slippage effect, the initiation pressure gradient, the pores' fractal characteristics, and water film mechanisms. Based on these models, we developed a three-region coupling productivity model for water-bearing tight gas reservoirs with multi-stage fractured horizontal wells. This productivity model considered the micro- and nano-scale effects and the heterogeneity of fracture networks. Then, the model was solved and validated with a field case. The results indicated that the three-region composite unsteady productivity model for water-bearing tight gas reservoirs, which incorporated micro- and nano-scale effects (with consideration of micro-scale and nano-scale phenomena in the fluid flow), could accurately predict a gas well's productivity. An analysis of the factors influencing productivity showed that ignoring the micro- and nano-scale effects in water-bearing tight gas reservoirs will underestimate the reservoir's productivity. The initial water saturation, the two-phase flow's initiation pressure gradient, and capillary force are all negatively correlated with the productivity of gas wells, while the conductivity of the fractures is positively correlated with gas well productivity.

Keywords: tight sandstone; relative gas–water permeability; productivity; micro- and nano-effects; fractal theory



Citation: Chen, F.; Duan, Y.; Wang, K. Productivity Model Study of Water-Bearing Tight Gas Reservoirs Considering Micro- to Nano-Scale Effects. *Processes* **2024**, *12*, 1499. <https://doi.org/10.3390/pr12071499>

Academic Editor: Qingbang Meng

Received: 3 June 2024

Revised: 9 July 2024

Accepted: 13 July 2024

Published: 17 July 2024



Copyright: © 2024 by the authors. Licensee MDPI, Basel, Switzerland. This article is an open access article distributed under the terms and conditions of the Creative Commons Attribution (CC BY) license (<https://creativecommons.org/licenses/by/4.0/>).

1. Introduction

China's tight sandstone gas reservoirs hold immense resources, making them the most abundant source of unconventional natural gas [1]. Due to the characteristics of tight sandstone, such as low porosity (the fraction of void space in the rock), low permeability (the ability of the rock to transmit fluids), complex pore throats (the narrow channels connecting larger pores), high capillary pressure (the pressure difference across the interface of two immiscible fluids in the pores), and high initial water saturation (the initial volume fraction of water in the pore space), the gas–water two-phase flow is complex. Relative permeability is an effective tool for studying multi-phase fluid flow in porous media [2]. Therefore, researching the relative gas–water permeability curves of tight sandstone reservoirs is of great significance for evaluating gas wells' productivity and achieving efficient development of tight sandstone gas reservoirs.

For conventional reservoirs, relatively reliable relative permeability curves can generally be obtained through laboratory core experiments (steady-state or unsteady-state

methods). However, due to the low porosity and permeability of tight sandstone, the steady-state method takes a long time to reach stability and is quite complex to operate, so it is rarely used. As for the unsteady-state method, the high heterogeneity and the abundance of micron-sized pores in tight sandstone make the release of gas through fractures likely. This makes unsteady-state displacement experiments difficult to conduct, and the experimental results are greatly influenced by human factors and the calculation methods [3]. The lattice Boltzmann simulation is a feasible method for obtaining the phase infiltration curves of tight sandstone. However, this method requires significant computational resources and time, and the range of pore sizes simulated is usually quite small, limiting its practical application [4]. Moreover, due to the limitations of the lattice Boltzmann method in handling fluid–solid boundary interactions, it is challenging to accurately account for factors such as water films, threshold pressure, and stress sensitivity during simulations. Therefore, establishing analytical models based on ideal pore structures and considering different displacement mechanisms not only aids in understanding the two-phase flow mechanism of gas and water but also provides a convenient and practical approach [5].

Klinkenberg derived a model for assessing apparent permeability in porous media based on the capillary bundle model [6]. Fulton experimentally investigated the effect of water saturation on the gas phase's permeability, and the results showed that the gas slippage effect decreased with an increase in water saturation [7]. Turgay developed a single-well productivity model considering the slippage effect, finding that gas reservoirs' recovery could increase by 5% to 8% under single-phase conditions when the slippage effect was considered [8]. Shi et al. established an analytical model for assessing the apparent permeability of the gas phase in tight sandstone under different levels of bound water saturation [9]. These research findings have revealed the flow mechanisms in the two-phase flow of gas and water, enhancing our understanding of productivity and the factors influencing fractured horizontal wells in tight sandstone gas reservoirs.

Jiao used the lattice Boltzmann method (LBM) and a discrete element method (DEM) to develop a novel pore-scale thermal–hydro–mechanical (THM) model, achieving accurate calculations of the flow of fluid and the temperature in fractures, as well as conducting a preliminary investigation of the THM fracturing mechanism [10]. Huang used finite-element and finite-difference methods to establish a quantitative correlation model between fracturing interference and horizontal wells' productivity, achieving better predictions for horizontal wells' productivity [11]. Yao et al. quantified the impact of water saturation on the threshold pressure gradient through experimental methods and established a model of two-phase gas–water flow for fractured horizontal wells. This model considered the effects of water saturation on the relative gas–water permeability, the threshold pressure gradient, and dynamic changes in the water–gas ratio [12]. Wei et al. pointed out that due to the high water saturation in tight sandstone gas reservoirs, factors such as the threshold pressure gradient and stress sensitivity have a significant impact on permeability. They developed an equation for calculating gas wells' productivity under steady-state flow conditions, considering the impact of water saturation on various mechanisms of permeability [13]. Lv et al. developed a productivity model for gas and water in horizontal wells in tight fractured gas reservoirs. This model comprehensively considered the characteristics of two-phase gas–water flow in the reservoir's matrix and fracture network, used a trilinear flow model to represent the impact of hydraulic fracturing, and accounted for the stress sensitivity of the reservoir's matrix and fractures. The model's predictions were compared with results from commercial numerical simulation software and production data from actual wells, verifying its accuracy [14]. Hu et al. proposed a numerical model of three-region flow and a power-law model of decline for calculating the productivity of fractured horizontal wells but did not consider the impact of the complex fracture network around the main fracture [15]. Therefore, due to the micro- and nano-scale of the pore throats in the tight sandstone reservoir matrix, factors such as the gas slippage effect, the threshold pressure gradient, stress sensitivity, and water films [16] have significant impacts on gas transport in the pore throats and should not be ignored in the establishment of practical models.

In addition, in actual low-permeability reservoirs, the interaction between natural fractures and hydraulic fractures generates secondary fractures, resulting in a complex fracture network. Therefore, further research is necessary in order to understand the impact of these complex fracture networks on the productivity of hydraulically fractured horizontal wells. Earlier productivity prediction models have not accounted for the interconnected complex fracture network formed by the primary fractures from hydraulic fracturing and natural fractures. Some models introduced idealized dual-porosity media to represent complex fracture networks, but this did not accurately reflect the actual heterogeneous fracture network structure. Although some studies have considered the heterogeneous morphological characteristics of fracture networks, the description of the non-uniform distribution of fracture networks remains unclear.

Given that current analytical models do not consider the combined effects of multiple mechanisms in tight gas reservoirs, such as comprehensive transport and micro- and nano-scale effects on productivity, and that the description of the non-uniform distribution of fracture networks is unclear, this study proposes a new analytical method based on permeation mechanics and fractal theory. Considering that the pore scale in tight gas reservoirs ranges from nanometers to micrometers, this study first establishes relative permeability models for micropores and nanopores, while comprehensively accounting for factors such as the gas slippage effect, the threshold pressure gradient, pore structure parameters, and water films. Subsequently, a new model for the multi-stage fracturing of tight gas reservoirs is developed, considering the influence of micro- and nano-scale effects and the heterogeneous characteristics of fracture networks on gas–water productivity. This model integrates mechanisms such as the slippage effect, stress sensitivity, and the threshold pressure gradient into the gas–water transport process. Finally, the productivity model is solved and validated with examples, and an analysis of the factors affecting gas well productivity is conducted. This not only enhances the understanding of gas–water two-phase flow dynamics but also provides a practical and effective tool for real-world applications, offering a comprehensive theoretical basis for accurately simulating gas–water flow in tight gas reservoirs.

2. Micropore Flow Model

In this section, the Hagen–Poiseuille equation [17] and a second-order slip model are employed to develop a gas–water flow model in micrometer-scale pores, incorporating boundary coupling conditions. This model, which accounts for the effects of pressure and temperature on fluid dynamics, accurately describes the flow of fluids in tight sandstone pores.

2.1. Establishment and Solution of Water Flow Model for Micropore Characterization Unit

The flow of water at the microscopic pore scale is assumed to be laminar (see Figure 1), and the velocity distribution of the fluid along the pipe diameter adheres to the fluid continuity principle [18].

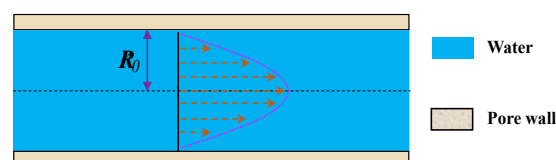


Figure 1. Flow velocity distribution of single-phase water in a micro-scale capillary tube.

The water molecules are assumed to have zero velocity at the wall, i.e., there is no slip. The water-phase flow rate in micropores can be represented by the traditional Hagen–Poiseuille equation [17]:

$$q_{w\mu m} = \int_0^{R_0} V_w dA_R = \frac{\Delta P}{L} \frac{\pi}{8\mu_w} R_0^4 \quad (1)$$

For single-phase water flow in tight gas reservoirs, boundary effects occur in hydrophilic micrometer tubes due to the strong interactions between the water phase and the solid phase [19]. This boundary layer effect is the primary cause of nonlinear flow. Based on previous studies, the initiation pressure and stress sensitivity are significant factors in the nonlinear flow of tight gas reservoirs. Therefore, it is necessary to further refine Equation (1).

2.1.1. Initiation Pressure Gradient and Stress Sensitivity

In tight gas reservoirs, the fluid flow must overcome the initiation gradient caused by surface molecular forces and capillary forces and exhibit distinctive non-Darcy seepage characteristics compared to conventional gas reservoirs. The relationship between flow rate and pressure gradient is notably nonlinear, introducing the non-Darcy flow rate of the initiation pressure gradient: when $\Delta P/L \leq g_w$ (g_w is the initiation pressure gradient of the water phase), the fluid does not flow, and when $\Delta P/L > g_w$, the fluid starts to flow.

During exploitation, the pressure in tight gas reservoirs continuously decreases. Under the influence of overlying pressure, the pore radius decreases, resulting in reductions in porosity and permeability. Based on the stress experiments on tight reservoirs by Dong et al. [20], a power-law relationship is used to characterize the relationship between pore radius and pressure:

$$R_s = R[(P_0 - P)/P_a]^{0.5(\phi_s - k_s)} \quad (2)$$

Based on this, considering the combined effects of the initiation pressure gradient and stress sensitivity, the velocity distribution of the water phase across the pipe diameter is

$$V_w = \left(\frac{\Delta P}{L} - g_w \right) \frac{1}{4\mu_w} (R_{0s}^2 - R_s^2) \quad (3)$$

By integrating along the capillary with a radius of R_0 , the water-phase flow equation considering the combined effects of initiation pressure gradient and stress sensitivity can be obtained as

$$q_{w\mu m} = \int_0^{R_{0s}} V_w dA_R = \left(\frac{\Delta P}{L} - g_w \right) \frac{\pi}{8\mu_w} R_{0s}^4 \quad (4)$$

In the above equation, R_{0s} is the pore radius, m, corresponding to a pressure P_0 .

2.1.2. Water-Phase Flow Rate of Characterization Unit Based on Fractal Theory

Pores in porous media exhibit fractal self-similarity characteristics across scales, from the nanometer scale to the micrometer scale [21]. According to fractal geometry theory, the fractal dimension of pore distribution can be calculated using the following equation [22]:

$$D_m = d - \frac{\ln \phi}{\ln(R_{\min}/R_{\max})} \quad (5)$$

where the fractal dimension of the pore distribution, labeled D_m , is a dimensionless number characterizing the complexity of the pore structure, typically ranging between 2 and 3 in three-dimensional pore structures; porosity, ϕ , indicates the proportion of pores in a rock relative to the total volume. The total number of pores between the minimum pore size R_{\min} and the maximum pore size R_{\max} is

$$n = (R_{\max}/R_{\min})^{D_m} \quad (6)$$

The probability density function of the distribution of pores with different pore sizes is given by [23]

$$f(R) = D_m R_{\min}^{D_m} / R^{(D_m+1)} \quad (7)$$

In porous media, the actual path of a pore varies due to its tortuous nature. A characterization unit of length L_0 is used to represent the properties of porous media, while

the actual length of the capillary L is greater than L_0 . The value of L can be derived from the following equation [24]:

$$L(R) = (2R)^{1-D_t} L_0^{D_t} \quad (8)$$

where D_t is the tortuosity fractal dimension, and for a three-dimensional characterization unit, $1 < D_t < 3$. $D_t = 1$ means a straight-line capillary, and $D_t = 3$ indicates that the capillary is infinitely tortuous and can fill the entire space. The tortuosity fractal dimension can be expressed as follows [25]:

$$D_t = 1 + \ln \left\{ \frac{1}{2} \left[1 + \frac{\sqrt{1-\phi}}{2} + \frac{\sqrt{1-\phi}}{1-\sqrt{1-\phi}} \sqrt{\left(\frac{1}{\sqrt{1-\phi}} - 1 \right)^2 + \frac{1}{4}} \right] \right\} / \ln \left\{ \frac{D_m - 1}{D_m^{0.5}} \sqrt{\frac{\pi}{8 - 4D_m} \frac{1-\phi}{\phi} \frac{R_{\max}}{R_{\min}}} \right\} \quad (9)$$

The capillary bundle model describes fluid flow paths in tight sandstone through a set of meandering capillary tubes of different diameters, effectively reflecting non-homogeneity. The capillary bundles are usually aligned perpendicular to the characterization unit, and the fluid can only flow through the capillary bundles, with no fluid flow occurring around the characterization unit (see Figure 2). The pore size distribution and tortuosity of this model conform to the descriptions of fractal theory. The hydrophilic nature of tight sandstone implies that capillary forces are significant in smaller pores, making it difficult for gas to enter these pores. Assuming that under a certain displacement pressure, there is a specific water saturation corresponding to a critical capillary radius, R_{cr} , pores with a radius smaller than R_{cr} exhibit single-phase water flow, while those with a radius larger than R_{cr} exhibit single-phase gas flow [26]. Since the water film thickness in actual tight sandstone reservoirs generally ranges from 1 to 20 nm [27], which can be ignored for micrometer-scale capillaries, it is assumed here that there is no water film in capillaries with a radius larger than the critical radius R_{cr} .

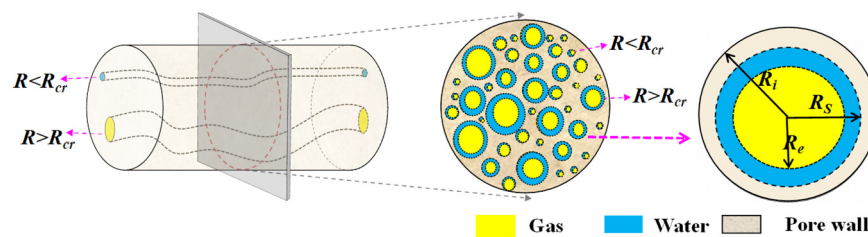


Figure 2. Schematic diagram of gas and water distribution in a tight sandstone core.

Based on the above assumptions, the equation for water saturation can be expressed as

$$S_w = \int_{R_{\min}}^{R_{cr}} \pi R^2 f(R) dR / \int_{R_{\min}}^{R_{\max}} \pi R^2 f(R) dR \quad (10)$$

By introducing pore radius tortuosity, initiation pressure gradient, and stress sensitivity, the single-phase water flow rate in a capillary tube can be expressed as

$$q_{w\mu m} = \int_0^{R_{0S}} V_w dA_R = \left(\frac{\Delta P_w}{L(R)} - g_w \right) \frac{\pi}{8\mu_w} R_{0S}^4 \quad (11)$$

Considering the effect of stress sensitivity, the maximum pore radius corresponding to R_{max} is R_{maxS} , the minimum pore radius corresponding to R_{min} is R_{minS} , and the critical capillary radius corresponding to R_{cr} is R_{crS} . The initiation pressure gradient is a constant value. By integrating Equation (11) from the capillary radius R_{minS} to R_{crS} , a new water-phase volume flow rate for the micropore characterization unit, which considers pore radius tortuosity, initiation pressure gradient, and stress sensitivity, can be obtained:

$$Q_{w\mu m} = n \int_{R_{minS}}^{R_{crS}} \left(\frac{\Delta P_w}{L(R)} - g_w \right) \frac{\pi}{8\mu_w} R^4 f(R) dR = \frac{\pi R_{maxS}^{D_m} D_m}{8\mu_w} \left[\frac{\Delta P_w}{2^{1-D_t} L_0^{D_t}} \frac{(R_{crS}^{D_t-D_m+3} - R_{minS}^{D_t-D_m+3})}{D_t - D_m + 3} - g_w \frac{(R_{crS}^{4-D_m} - R_{minS}^{4-D_m})}{4 - D_m} \right] \quad (12)$$

2.2. Establishment and Solution of Gas Flow Model for Micropore Characterization Unit

In micropores, the gas-phase flow is laminar, and the velocity distribution follows the gas-phase continuity equation [17]:

$$\frac{\mu_g}{R} \frac{\partial}{\partial R} \left(R \frac{\partial V_{g\mu m}}{\partial R} \right) = \frac{\partial P}{\partial z} \quad (13)$$

where g denotes the gas phase; the other parameters have the same meaning as those described for the water phase.

When the Knudsen number increases above 0.001, due to gas-gas and gas-solid interactions, the kinetic energy transfer of gas molecules near the wall becomes complex. Some gas molecules do not adhere completely to the pipe wall, exhibiting a slip phenomenon, which significantly impacts gas transport [28]. Under conditions where the Knudsen number is below 0.1, the second-order slip model [29] can accurately describe the slip velocity at the wall.

$$V_{gs} = \left(A_1 \lambda \frac{\partial V_g}{\partial R} - A_2 \lambda^2 \frac{\partial^2 V_g}{\partial R^2} \right) \Big|_{R=R_0} \quad (14)$$

where A_1 and A_2 are the first- and second-order slip coefficients, respectively, with A_1 taking the value of $4/3$ and A_2 taking the value of $1/4$ [29]; and λ is the mean free path of gas molecules [30].

Considering the gas-phase slip effect, the gas-phase flow rate differs from the water-phase flow rate (see Figure 3).

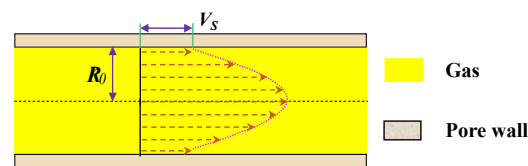


Figure 3. Flow velocity distribution of single-phase gas in a micro-scale capillary tube.

Figure 3 shows the velocity profile of gas flowing through a micro-scale capillary, taking into account slip effects, the initiation pressure gradient, and stress sensitivity. The distribution highlights the nonlinear flow characteristics unique to tight gas reservoirs.

Thus, the boundary condition for single-phase gas flow can be expressed as follows:

$$\frac{\partial V_{g\mu m}}{\partial R} \Big|_{R=R_0} = 0, V_{g\mu m} \Big|_{R=R_0} = V_w \Big|_{R=R_0} + V_{gs} \Big|_{R=R_0} \quad (15)$$

The slip effect, initiation pressure, and stress sensitivity in tight gas reservoirs are significant and cannot be ignored. Similar to the water-phase model derivation, by introducing pore radius tortuosity based on fractal theory, the gas-phase velocity distribution and gas-phase flow rate equation, which comprehensively consider boundary slippage, initiation pressure, and stress sensitivity for micropores, can be obtained as follows:

$$V_{g\mu m} = \frac{1}{4\mu_g} \left(\frac{\Delta P}{L} - g_g \right) \left(R_{0s}^2 + 2A_1 \lambda R_{0s} - 2A_2 \lambda^2 - R_s^2 \right) \quad (16)$$

$$q_{g\mu m} = \int_0^{R_{0s}} V_{g\mu m} dA_R = \frac{\pi}{8\mu_g} \left(\frac{\Delta P_g}{L(R)} - g_g \right) \left(R_{0s}^4 + 4A_1 \lambda R_{0s}^3 - 4A_2 \lambda^2 R_{0s}^2 \right) \quad (17)$$

The extra first-order slip term and the second-order slip term account for the differences in the flow expressions due to slippage.

Considering the influence of stress sensitivity and assuming that the gas-phase initiation pressure gradient is constant, by integrating the capillary radius from R_{crs} to R_{maxs} in Equation (17), a new gas-phase volume flow rate for the micropore characterization

unit, which comprehensively considers pore radius tortuosity, gas-phase initiation pressure gradient, and stress sensitivity, can be obtained:

$$Q_{gum} = n \int_{R_{crS}}^{R_{maxS}} q_{gum} f(R) dR = \frac{\pi R_{maxS}^{D_m} D_m}{8 \mu_g} \left[\frac{\Delta P_g}{2^{1-D_t} L_0^{D_t}} \left(\frac{R_{maxS}^{D_t-D_m+3} - R_{crS}^{D_t-D_m+3}}{D_t - D_m + 3} + 4A_1 \lambda \frac{R_{maxS}^{D_t-D_m+2} - R_{crS}^{D_t-D_m+2}}{D_t - D_m + 2} - 4A_2 \lambda^2 \frac{R_{maxS}^{D_t-D_m+1} - R_{crS}^{D_t-D_m+1}}{D_t - D_m + 1} \right) - g_g \left(\frac{R_{maxS}^{4-D_m} - R_{crS}^{4-D_m}}{4 - D_m} + 4A_1 \lambda \frac{R_{maxS}^{3-D_m} - R_{crS}^{3-D_m}}{3 - D_m} - 4A_2 \lambda^2 \frac{R_{maxS}^{2-D_m} - R_{crS}^{2-D_m}}{2 - D_m} \right) \right] \quad (18)$$

2.3. Relative Permeability Model

According to the gas–water two-phase flow distribution, the expression for water saturation can be obtained as follows:

$$S_w = \frac{\int_{R_{minS}}^{R_{crS}} \pi R^2 f(R) dR}{\int_{R_{minS}}^{R_{maxS}} \pi R^2 f(R) dR} = \frac{R_{crS}^{-D_m+2} - R_{minS}^{-D_m+2}}{R_{maxS}^{-D_m+2} - R_{minS}^{-D_m+2}} \quad (19)$$

In addition, flow rates in the water and gas phases can be expressed using the Darcy expansion equation [25]:

$$Q_{wum} = -\frac{K_w}{\mu_w} \frac{A}{S_w} \frac{\Delta P_w}{L_0} \quad Q_{gum} = -\frac{K_g}{\mu_g} \frac{A}{(1 - S_w)} \frac{\Delta P_g}{L_0} \quad (20)$$

By combining Equations (12) and (18)–(20), the effective permeability of water and gas in micropores can be obtained, respectively:

$$K_w = -S_w \frac{\phi}{(1 - \phi)} \frac{R_{maxS}^{D_m-2} (2 - D_m)}{8} \left[\frac{\Delta P_w}{2^{1-D_t} L_0^{D_t-1}} \frac{(R_{crS}^{D_t-D_m+3} - R_{minS}^{D_t-D_m+3})}{D_t - D_m + 3} - \frac{g_w}{L_0} \frac{(R_{crS}^{4-D_m} - R_{minS}^{4-D_m})}{4 - D_m} \right] \quad (21)$$

$$K_g = -(1 - S_w) \frac{\phi}{(1 - \phi)} \frac{R_{maxS}^{D_m-2} (2 - D_m)}{8} \times \left[\frac{\Delta P_g}{2^{1-D_t} L_0^{D_t-1}} \left(\frac{R_{maxS}^{D_t-D_m+3} - R_{crS}^{D_t-D_m+3}}{D_t - D_m + 3} + 4A_1 \lambda \frac{R_{maxS}^{D_t-D_m+2} - R_{crS}^{D_t-D_m+2}}{D_t - D_m + 2} - 4A_2 \lambda^2 \frac{R_{maxS}^{D_t-D_m+1} - R_{crS}^{D_t-D_m+1}}{D_t - D_m + 1} \right) - \frac{g_g}{L_0} \left(\frac{R_{maxS}^{4-D_m} - R_{crS}^{4-D_m}}{4 - D_m} + 4A_1 \lambda \frac{R_{maxS}^{3-D_m} - R_{crS}^{3-D_m}}{3 - D_m} - 4A_2 \lambda^2 \frac{R_{maxS}^{2-D_m} - R_{crS}^{2-D_m}}{2 - D_m} \right) \right] \quad (22)$$

When Equation (21) satisfies the condition $S_w = 1$, the absolute permeability of the core can be obtained:

$$K_w = -\frac{\phi}{(1 - \phi)} \frac{R_{maxS}^{D_m-2} (2 - D_m)}{8} \left[\frac{\Delta P_w}{2^{1-D_t} L_0^{D_t-1}} \frac{(R_{maxS}^{D_t-D_m+3} - R_{minS}^{D_t-D_m+3})}{D_t - D_m + 3} - \frac{g_w}{L_0} \frac{(R_{maxS}^{4-D_m} - R_{minS}^{4-D_m})}{4 - D_m} \right] \quad (23)$$

Therefore, the relative permeability of gas and water in the micropores of a tight sandstone reservoir can be expressed as follows:

$$K_{rw} = S_w \left(\frac{R_{crS}^{D_t-D_m+3} - MR_{crS}^{4-D_m}}{R_{maxS}^{D_t-D_m+3} - MR_{maxS}^{4-D_m}} \right) \quad (24)$$

$$K_{rg} = \frac{(1 - S_w)}{C_3 \frac{R_{maxS}^{D_t-D_m+3}}{D_t - D_m + 3} - C_2 \frac{R_{maxS}^{4-D_m}}{4 - D_m}} \left[C_1 \left(\frac{R_{maxS}^{D_t-D_m+3} - R_{crS}^{D_t-D_m+3}}{D_t - D_m + 3} + 4A_1 \lambda \frac{R_{maxS}^{D_t-D_m+2} - R_{crS}^{D_t-D_m+2}}{D_t - D_m + 2} - 4A_2 \lambda^2 \frac{R_{maxS}^{D_t-D_m+1} - R_{crS}^{D_t-D_m+1}}{D_t - D_m + 1} \right) - \right] \quad (25)$$

where $M = \frac{g_w}{L_0} \frac{D_t - D_m + 3}{4 - D_m} \frac{2^{1-D_t} L_0^{D_t-1}}{\Delta P_w}$, $C_1 = g_g \frac{2^{1-D_t} L_0^{D_t-2}}{\Delta P_g}$, $C_2 = g_w \frac{2^{1-D_t} L_0^{D_t-2}}{\Delta P_g}$, $C_3 = \frac{\Delta P_w}{\Delta P_g}$.

3. Nanopore Flow Model

Nanopores are widely present in tight sandstone, and due to their hydrophilic nature, film flow is a common pattern in hydrophilic nanopores. This must be considered in nanopores [27]. In this section, a two-phase gas–water flow model in nanopores is

established, considering the gas slippage effect, water film thickness, and the high-viscosity water film layer. The model also considers stress sensitivity and initiation pressure gradient.

3.1. Establishment and Solution of Water Flow Model for Nanopore Characterization Unit

The flow in nanopores is more complex, with more pronounced boundary layer effects. The contact between the water phase and the solid phase can be divided into a high-viscosity water phase and a conventional-viscosity water phase [31]. A schematic diagram of single-phase water flow in hydrophilic nanopores is shown in Figure 4a. It is assumed that the water phase with conventional viscosity is located away from the pore wall, with a radius of R_δ , while the high-viscosity water phase is near the pore wall, with a radius of $R_0 - R_\delta$. A schematic diagram of gas–water two-phase flow in hydrophilic nanopores is shown in Figure 4b. The gas phase is in the center of the capillary, with a radius of R_{gw} . Near the gas phase is the conventional-viscosity water phase, with a thickness of $R_\delta - R_{gw}$, and near the pore wall is the high-viscosity water phase, with a thickness of $R_0 - R_{gw}$.

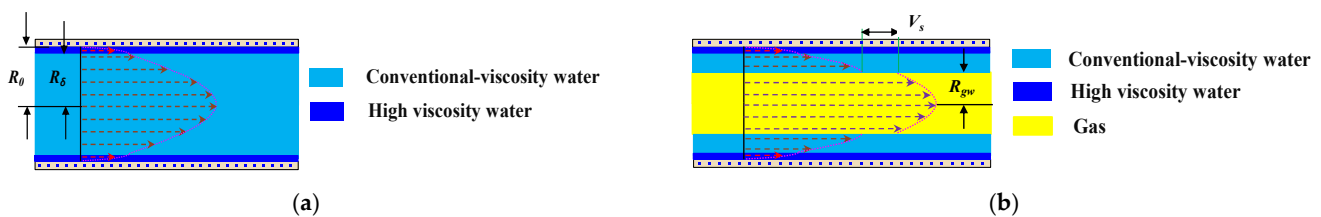


Figure 4. Velocity distribution in nanopores. (a) Velocity distribution of single-phase water in nanopores. (b) Velocity distribution of gas and water phases in nanopores.

These schematic diagrams illustrate the flow dynamics within hydrophilic nanopores, considering the boundary layer effects and differences in viscosity near the pore walls, which are crucial for understanding fluid behavior at the nanometer scale.

The flow of each phase fluid in various regions of a nanotube still satisfies the Hagen–Poiseuille equation [17]. After applying the boundary conditions, the governing equations for the conventional-viscosity water phase and the high-viscosity water phase can be expressed as follows, respectively:

$$V_{1w} = -\frac{\Delta P}{L} \frac{1}{4\mu_{w1}} R^2 + A_{w1}, R \in [R_{gw}, R_\delta], V_{2w} = -\frac{\Delta P}{L} \frac{1}{4\mu_{w2}} R^2 + A_{w2}, R \in [R_\delta, R_0] \quad (26)$$

Under strongly hydrophilic conditions, $\mu_{w2} = 3.25\mu_{w1}$ [32]; A is a constant; and the subscripts w_1, w_2 denote the regular-viscosity water-phase region and the high-viscosity water-phase region, respectively. If $R_{gw} = 0$, it means that single-phase water flow is occurring in the capillary.

The boundary conditions satisfy velocity continuity, conservation of mass, and a shear relationship:

$$\begin{cases} V_{1w} \big|_{R=R_\delta} = V_{2w} \big|_{R=R_\delta} \\ \mu_{w1} \frac{\partial V_{1w}}{\partial R} \big|_{R=R_\delta} = \mu_{w2} \frac{\partial V_{2w}}{\partial R} \big|_{R=R_\delta} \\ V_{2w} \big|_{R=R_0} = 0 \end{cases} \quad (27)$$

Combining Equations (26) and (27), the velocity equations for the conventional-viscosity water phase and the high-viscosity water phase can be obtained. The initiation pressure and stress sensitivity in tight gas reservoirs, especially in nanopores, cannot be ignored. Based on the derivation in the previous section, stress sensitivity is represented by a power-law relationship that characterizes the relationship between pore radius and pressure as in Equation (2). The water-phase velocity distribution in the conventional-viscosity

and high-viscosity water-phase regions of nanopores, considering initiation pressure and stress sensitivity, can be obtained as follows:

$$V_{1w} = \left(\frac{\Delta P}{L} - g_w \right) \left(\frac{R_{\delta S}^2 - R_S^2}{4\mu_{w1}} + \frac{R_{0S}^2 - R_{\delta S}^2}{4\mu_{w2}} \right), R_S \in [R_{gws}, R_{\delta S}] \quad (28)$$

$$V_{2w} = \left(\frac{\Delta P}{L} - g_w \right) \frac{1}{4\mu_{w2}} (R_{0S}^2 - R_S^2), R_S \in [R_{\delta S}, R_{0S}] \quad (29)$$

In the above equation, $R_{\delta S}$, R_{gws} , R_{0S} , and R_S correspond to the aperture diameters of R_{δ} , R_{gw} , R_0 , and R under stress sensitivity, respectively, m.

By integrating the capillary radius in the respective water-phase regions in Equations (28) and (29), and considering that the capillary radius and tortuosity follow fractal theory, the water-phase flow rate formula in nanopores, accounting for initiation pressure and stress sensitivity, can be obtained as follows:

$$q_{wnm} = \int_{R_{gws}}^{R_{\delta S}} V_{1w} dA_r + \int_{R_{\delta S}}^{R_{0S}} V_{2w} dA_r = \left(\frac{\Delta P_w}{L(R)} - g_w \right) \left(\frac{\pi(R_{\delta S}^2 - R_{gws}^2)^2}{8\mu_{w1}} + \frac{\pi[R_{0S}^4 - R_{\delta S}^4 - 2(R_{0S}^2 - R_{\delta S}^2)R_{gws}^2]}{8\mu_{w2}} \right) \quad (30)$$

When there is only single-phase water flow in the capillary, $R_{gw} = 0$, the water-phase equation can be simplified as

$$q_{wnm} = \int_0^{R_{\delta S}} V_{1w} dA_R + \int_{R_{\delta S}}^{R_{0S}} V_{2w} dA_R = \left(\frac{\Delta P_w}{L(R)} - g_w \right) \left(\frac{\pi R_{\delta S}^4}{8\mu_{w1}} + \frac{\pi(R_{0S}^4 - R_{\delta S}^4)}{8\mu_{w2}} \right) \quad (31)$$

For gas–water two-phase flow in hydrophilic tight sandstone pores, it is assumed that there is a critical capillary radius R_{cr} . When $R < R_{cr}$, there is a single-phase water flow pattern; when $R > R_{cr}$, the capillary exhibits a “gas core water film” flow pattern [16]. Therefore, the water saturation of the nanopore characterization unit can be expressed as follows:

$$S_w = \frac{n \int_{R_{minS}}^{R_{crS}} \pi R_S^2 f(R) dR + n \int_{R_{crS}}^{R_{maxS}} \pi (R_S^2 - R_{gws}^2) f(R) dR}{n \int_{R_{minS}}^{R_{maxS}} \pi R_S^2 f(R) dR} \quad (32)$$

Based on the assumption, the volume flow rate of the water phase consists of single-phase water flow with pore radius $R < R_{cr}$ and water film flow with pore radius $R > R_{cr}$. The water-phase volume flow rate can be derived from Equations (7) to (8) and Equations (30) to (31). Based on the assumption, the volume flow rate of the water phase consists of two parts:

$$Q_{wnm} = n \int_{r_{minS}}^{r_{maxS}} q_{wnm} f(R) dR = \frac{\pi R_{maxS}^{D_m} D_m}{8} \left\{ \begin{array}{l} \left[\frac{\Delta P_w}{2^{1-D_i} L_0^{D_i}} \left[\int_{R_{minS}}^{R_{crS}} \left(\frac{R_{\delta S}^4}{\mu_{w1}} + \frac{R_S^4 - R_{\delta S}^4}{\mu_{w2}} \right) R_S^{D_i - D_m - 2} dR_S \right. \right. \\ \left. \left. + \int_{R_{crS}}^{R_{maxS}} \left(\frac{(R_{\delta S}^2 - R_{gws}^2)^2}{\mu_{w1}} + \frac{[R_S^4 - R_{\delta S}^4 - 2(R_S^2 - R_{\delta S}^2)R_{gws}^2]}{\mu_{w2}} \right) R_S^{D_i - D_m - 2} dR_S \right] \right. \\ \left. - g_w \left[\int_{R_{minS}}^{R_{crS}} \left(\frac{R_{\delta S}^4}{\mu_{w1}} + \frac{R_S^4 - R_{\delta S}^4}{\mu_{w2}} \right) R_S^{-D_m - 1} dR_S \right. \right. \\ \left. \left. + \int_{R_{crS}}^{R_{maxS}} \left(\frac{(R_{\delta S}^2 - R_{gws}^2)^2}{\mu_{w1}} + \frac{[R_S^4 - R_{\delta S}^4 - 2(R_S^2 - R_{\delta S}^2)R_{gws}^2]}{\mu_{w2}} \right) R_S^{-D_m - 1} dR_S \right] \right] \end{array} \right\} \quad (33)$$

The above equation represents the water-phase volume flow rate for the nanopore characterization unit, comprehensively considering pore radius tortuosity, initiation pressure gradient, and stress sensitivity.

3.2. Nanopore Characterization Unit Gas Flow Model and Solution

For gas flow in nanotubes, the fluid still satisfies the Hagen–Poiseuille equation [17], and the governing equation for the gas phase is

$$V_{gnm} = -\frac{\Delta P}{L} \frac{1}{4\mu_g} R^2 + A_g, R \in [0, R_{gw}] \quad (34)$$

where subscript g denotes the gas-phase region, and there is single-phase flow when $R_{gw} = 0$. The boundary conditions satisfy velocity continuity and mass conservation:

$$\begin{cases} \frac{\partial V_{gnm}}{\partial R} \Big|_{R=0} = 0 \\ V_{gnm} \Big|_{R=R_{gw}} = V_{1w} \Big|_{R=R_{gw}} + V_{gs} \Big|_{R=R_{gw}} \end{cases} \quad (35)$$

where V_s is the slip velocity at the wall, m/s. Since the slip effect of the gas is not negligible when the Knudsen number is greater than 0.01, the slip boundary condition proposed by Karnidakis et al. [29] is adopted here. It can characterize gas transport across the entire range of Knudsen numbers:

$$V_s = \frac{\lambda}{1 - c\lambda} \frac{2 - \tau_v}{\tau_v} \left(\frac{\partial V_{gnm}}{\partial R} \right) \Big|_{R_{wall}} \quad (36)$$

where c is the slip coefficient, $c = -1$, with second-order accuracy; τ_v is the tangential momentum coordination coefficient, $\tau_v = 1$; and λ is the mean free path of gas molecules [31].

As discussed in the previous section, there is an initiation pressure gradient at the point of gas–liquid contact in tight gas reservoirs. Considering stress sensitivity (Equation (2)), and combining Equations (34), (36), and the boundary condition Equation (35), a new expression for gas-phase velocity in nano-scale pores can be obtained:

$$V_{gnm} = \left(\frac{\Delta P}{L} - g_g \right) \frac{1}{4\mu_g} \left(R_{gws}^2 + \frac{2\lambda}{1 - c\lambda} \frac{2 - \tau_v}{\tau_v} R_{gws} - R_S^2 \right) + \left(\frac{\Delta P}{L} - g_g \right) \left(\frac{R_{\delta S}^2 - R_{gws}^2}{4\mu_{w1}} + \frac{R_{0S}^2 - R_{\delta S}^2}{4\mu_{w2}} \right), R_S \in [0, R_{gws}] \quad (37)$$

By integrating the above equation over the corresponding capillary radius regions and considering the influence of tortuosity, the gas-phase flow rate in a single nanopore can be obtained:

$$q_{gnm} = \int_0^{R_{gws}} V_{gnm} dA_{R_S} = \left(\frac{\Delta P_g}{L(R_S)} - g_g \right) \frac{\pi}{8\mu_g} \left(R_{gws}^4 + \frac{4\lambda}{1 - c\lambda} \frac{2 - \tau_v}{\tau_v} R_{gws}^3 \right) + \left(\frac{\Delta P_g}{L(R_S)} - g_g \right) \frac{\pi}{4\mu_{w1}} (R_{\delta S}^2 - R_{gws}^2) R_{gws}^2 + \left(\frac{\Delta P_g}{L(R_S)} - g_g \right) \frac{\pi}{4\mu_{w2}} (R_{0S}^2 - R_{\delta S}^2) R_{gws}^2 \quad (38)$$

Considering the effect of stress sensitivity and assuming a constant initiation pressure gradient for the gas phase, capillaries with a radius smaller than R_{cr} are primarily single-phase water flow, while those with a radius larger than R_{cr} exhibit gas flow [26]. The influence of the water film in nanopores cannot be ignored. By integrating Equation (38) over the capillary radius from R_{crS} to R_{maxS} , a new expression for the gas-phase volume flow rate in a nanopore, considering tortuosity, gas-phase initiation pressure gradient, and stress sensitivity, can be obtained:

$$Q_{gnm} = n \int_{R_{crS}}^{R_{maxS}} q_{gnm} f(R_S) dR_S = \frac{\pi R_{maxS}^{D_m} D_m}{8} \left\{ \begin{aligned} & \frac{\Delta P_g}{2^{1-D_t} L_0^{D_t}} \int_{R_{crS}}^{R_{maxS}} \left[\frac{1}{\mu_g} \left(R_{gws}^4 + \frac{4\lambda}{1 - c\lambda} \frac{2 - \tau_v}{\tau_v} R_{gws}^3 \right) + \right. \\ & \left. \frac{2}{\mu_{w1}} (R_{\delta S}^2 - R_{gws}^2) R_{gws}^2 + \frac{2}{\mu_{w2}} (R_S^2 - R_{\delta S}^2) R_{gws}^2 \right] R_S^{D_t - D_m - 2} dR_S \\ & - g_g \int_{R_{crS}}^{R_{maxS}} \left[\frac{1}{\mu_g} \left(R_{gws}^4 + \frac{4\lambda}{1 - c\lambda} \frac{2 - \tau_v}{\tau_v} R_{gws}^3 \right) + \right. \\ & \left. \frac{2}{\mu_{w1}} (R_{\delta S}^2 - R_{gws}^2) R_{gws}^2 + \frac{2}{\mu_{w2}} (R_S^2 - R_{\delta S}^2) R_{gws}^2 \right] R_S^{-D_m - 1} dR_S \end{aligned} \right\} \quad (39)$$

3.3. Relative Permeability Model

The water saturation of the characterization unit is obtained from Equation (32):

$$S_w = (2 - D_m) \frac{\int_{R_{minS}}^{R_{crS}} R_S^{-D_m + 1} dR_S + \int_{R_{crS}}^{R_{maxS}} (R_S^2 - R_{gws}^2) R_S^{-D_m + 1} dR_S}{(R_{maxS}^{-D_m + 2} - R_{minS}^{-D_m + 2})} \quad (40)$$

where K_g and K_w are the effective permeability of the gas and water phases, respectively, mD; and A is the cross-sectional area of the characterization unit, m³.

According to Equations (20) and (33), the effective permeability of the water and gas phases of the characterization unit can be obtained, respectively, as follows:

$$K_w = -\frac{S_w \mu_{w1} \pi R_{\max}^{D_m} D_m}{8A} \left\{ \frac{\Delta P_w}{2^{1-D_t} L_0^{D_t-1}} \left[\int_{R_{\min}^S}^{R_{cr}^S} \left(\frac{R_{\delta S}^4}{\mu_{w1}} + \frac{R_S^4 - R_{\delta S}^4}{\mu_{w2}} \right) R_S^{D_t - D_m - 2} dR_S \right. \right. \\ \left. \left. + \int_{R_{cr}^S}^{R_{\max}^S} \left(\frac{(R_{\delta S}^2 - R_{gws}^2)^2}{\mu_{w1}} + \frac{[R_S^4 - R_{\delta S}^4 - 2(R_{\delta S}^2 - R_{gws}^2)R_{gws}^2]}{\mu_{w2}} \right) R_S^{D_t - D_m - 2} dR_S \right] - \frac{g_w}{L_0} \left[\int_{R_{\min}^S}^{R_{cr}^S} \left(\frac{R_{\delta S}^4}{\mu_{w1}} + \frac{R_S^4 - R_{\delta S}^4}{\mu_{w2}} \right) R_S^{-D_m - 1} dR_S \right. \right. \\ \left. \left. + \int_{R_{cr}^S}^{R_{\max}^S} \left(\frac{(R_{\delta S}^2 - R_{gws}^2)^2}{\mu_{w1}} + \frac{[R_S^4 - R_{\delta S}^4 - 2(R_{\delta S}^2 - R_{gws}^2)R_{gws}^2]}{\mu_{w2}} \right) R_S^{-D_m - 1} dR_S \right] \right\} \quad (41)$$

$$K_g = -\frac{(1 - S_w) \mu_{gi} \pi R_{\max}^{D_m} D_m}{8A} \left\{ \frac{\Delta P_g}{2^{1-D_t} L_0^{D_t-1}} \int_{R_{cr}^S}^{R_{\max}^S} \left[\frac{1}{\mu_g} \left(R_{gws}^4 + \frac{4\lambda}{1-\epsilon\lambda} \frac{2-\tau_w}{\tau_w} R_{gws}^3 \right) + \right. \right. \\ \left. \left. \frac{2}{\mu_{w1}} (R_{\delta S}^2 - R_{gws}^2) R_{gws}^2 + \frac{2}{\mu_{w2}} (R_S^2 - R_{\delta S}^2) R_{gws}^2 \right] R_S^{D_t - D_m - 2} dR_S - \frac{g_w}{L_0} \int_{R_{cr}^S}^{R_{\max}^S} \left[\frac{1}{\mu_g} \left(R_{gws}^4 + \frac{4\lambda}{1-\epsilon\lambda} \frac{2-\tau_w}{\tau_w} R_{gws}^3 \right) + \right. \right. \\ \left. \left. \frac{2}{\mu_{w1}} (R_{\delta S}^2 - R_{gws}^2) R_{gws}^2 + \frac{2}{\mu_{w2}} (R_S^2 - R_{\delta S}^2) R_{gws}^2 \right] R_S^{-D_m - 1} dR_S \right\} \quad (42)$$

When $S_w = 1$ and $R_{gws} = 0$, single-phase water flow is found in the nanopore, and the absolute permeability of the nanopore characterization unit can be obtained as follows:

$$K = -\frac{S_w}{A} \mu_{w1} \frac{\pi R_{\max}^{D_m} D_m}{8} \left\{ \frac{\Delta P_w}{2^{1-D_t} L_0^{D_t-1}} \left[\int_{R_{\min}^S}^{R_{\max}^S} \left(\frac{R_{\delta S}^4}{\mu_{w1}} + \frac{R_S^4 - R_{\delta S}^4}{\mu_{w2}} \right) R_S^{D_t - D_m - 2} dR_S \right] - \frac{g_w}{L_0} \left[\int_{R_{\min}^S}^{R_{\max}^S} \left(\frac{R_{\delta S}^4}{\mu_{w1}} + \frac{R_S^4 - R_{\delta S}^4}{\mu_{w2}} \right) R_S^{-D_m - 1} dR_S \right] \right\} \quad (43)$$

According to Equation (43), the relative permeability of the water phase of the nanopore characterization unit can be obtained as follows:

$$K_{Rw} = K_{Rwcr} + K_{Rwm} = S_w \frac{\int_{R_{\min}^S}^{R_{cr}^S} \left(\frac{R_{\delta S}^4}{\mu_{w1}} + \frac{R_S^4 - R_{\delta S}^4}{\mu_{w2}} \right) R_S^{D_t - D_m - 2} dR_S - C_1 \int_{R_{\min}^S}^{R_{cr}^S} \left(\frac{R_{\delta S}^4}{\mu_{w1}} + \frac{R_S^4 - R_{\delta S}^4}{\mu_{w2}} \right) R_S^{-D_m - 1} dR_S}{\int_{R_{\min}^S}^{R_{\max}^S} \left(\frac{R_{\delta S}^4}{\mu_{w1}} + \frac{R_S^4 - R_{\delta S}^4}{\mu_{w2}} \right) R_S^{D_t - D_m - 2} dR_S - C_1 \int_{R_{\min}^S}^{R_{\max}^S} \left(\frac{R_{\delta S}^4}{\mu_{w1}} + \frac{R_S^4 - R_{\delta S}^4}{\mu_{w2}} \right) R_S^{-D_m - 1} dR_S} + S_w \times \\ \frac{\int_{R_{cr}^S}^{R_{\max}^S} \left(\frac{(R_{\delta S}^2 - R_{gws}^2)^2}{\mu_{w1}} + \frac{[R_S^4 - R_{\delta S}^4 - 2(R_{\delta S}^2 - R_{gws}^2)R_{gws}^2]}{\mu_{w2}} \right) R_S^{D_t - D_m - 2} dR_S - C_1 \int_{R_{cr}^S}^{R_{\max}^S} \left(\frac{(R_{\delta S}^2 - R_{gws}^2)^2}{\mu_{w1}} + \frac{[R_S^4 - R_{\delta S}^4 - 2(R_{\delta S}^2 - R_{gws}^2)R_{gws}^2]}{\mu_{w2}} \right) R_S^{-D_m - 1} dR_S}{\int_{R_{\min}^S}^{R_{\max}^S} \left(\frac{R_{\delta S}^4}{\mu_{w1}} + \frac{R_S^4 - R_{\delta S}^4}{\mu_{w2}} \right) R_S^{D_t - D_m - 2} dR_S - C_1 \int_{R_{\min}^S}^{R_{\max}^S} \left(\frac{R_{\delta S}^4}{\mu_{w1}} + \frac{R_S^4 - R_{\delta S}^4}{\mu_{w2}} \right) R_S^{-D_m - 1} dR_S} \quad (44)$$

where $C_1 = g_w 2^{1-D_t} L_0^{D_t-1} / (\Delta P_w L_0)$; and K_{Rwcr} and K_{Rwm} , respectively, represent the water-phase seepage contributed by pores with a radius smaller than R_{cr} and by pores with a radius larger than R_{cr} .

According to Equations (42) and (43), the relative permeability of the gas phase of the nanopore characterization unit can be obtained:

$$K_{Rg} = (1 - S_w) \frac{\mu_{gi}}{\mu_{w1}} \left\{ \frac{C_2 \int_{R_{cr}^S}^{R_{\max}^S} \left[\frac{1}{\mu_g} \left(R_{gws}^4 + \frac{4\lambda}{1-\epsilon\lambda} \frac{2-\tau_w}{\tau_w} R_{gws}^3 \right) \right] R_S^{D_t - D_m - 2} dR_S - C_3 \int_{R_{cr}^S}^{R_{\max}^S} \left[\frac{1}{\mu_g} \left(R_{gws}^4 + \frac{4\lambda}{1-\epsilon\lambda} \frac{2-\tau_w}{\tau_w} R_{gws}^3 \right) \right] R_S^{-D_m - 1} dR_S}{\int_{R_{\min}^S}^{R_{\max}^S} \left(\frac{R_{\delta S}^4}{\mu_{w1}} + \frac{R_S^4 - R_{\delta S}^4}{\mu_{w2}} \right) R_S^{D_t - D_m - 2} dR_S - C_1 \int_{R_{\min}^S}^{R_{\max}^S} \left(\frac{R_{\delta S}^4}{\mu_{w1}} + \frac{R_S^4 - R_{\delta S}^4}{\mu_{w2}} \right) R_S^{-D_m - 1} dR_S} + \right. \\ \left. \frac{C_2 \int_{R_{cr}^S}^{R_{\max}^S} \left[\frac{2}{\mu_{w1}} (R_{\delta S}^2 - R_{gws}^2) R_{gws}^2 + \frac{2}{\mu_{w2}} (R_S^2 - R_{\delta S}^2) R_{gws}^2 \right] R_S^{D_t - D_m - 2} dR_S - C_3 \int_{R_{cr}^S}^{R_{\max}^S} \left[\frac{2}{\mu_{w1}} (R_{\delta S}^2 - R_{gws}^2) R_{gws}^2 + \frac{2}{\mu_{w2}} (R_S^2 - R_{\delta S}^2) R_{gws}^2 \right] R_S^{-D_m - 1} dR_S}{\int_{R_{\min}^S}^{R_{\max}^S} \left(\frac{R_{\delta S}^4}{\mu_{w1}} + \frac{R_S^4 - R_{\delta S}^4}{\mu_{w2}} \right) R_S^{D_t - D_m - 2} dR_S - C_1 \int_{R_{\min}^S}^{R_{\max}^S} \left(\frac{R_{\delta S}^4}{\mu_{w1}} + \frac{R_S^4 - R_{\delta S}^4}{\mu_{w2}} \right) R_S^{-D_m - 1} dR_S} \right\} \quad (45)$$

where $C_2 = \Delta P_g / \Delta P_w$, $C_3 = g_g 2^{1-D_t} L_0^{D_t-1} / (\Delta P_w L_0)$.

3.4. Relative Permeability Model Validation

Although this study presents flow rates characterized by pore units of different scales, accurately measuring microscopic flow in both nanopores and micropores remains challenging. From a theoretical perspective and based on the derivation process, flow rate and relative permeability are closely related. Therefore, the derived two-phase flow relative permeability is used for model validation.

This section first compares the established micropore and nanopore relative permeability models with experimental and simulated gas–water relative permeability data from various sources. This comparison aims to verify the reliability of the micropore and nanopore relative permeability models.

The fractal dimension of the pore size distribution (D_m) and the fractal dimension of the tortuosity (D_t) are obtained from Equations (5) and (9). Some parameter values can be obtained based on experimental results. In the absence of experimental conditions, they can also be derived from previous research findings. The basis for gathering key parameters is elaborated as follows:

① Experimental Data and Previous Research: The values of key parameters such as pore radius, viscosity, and slip coefficients are derived from experimental studies and validated research findings. For example, the molecular diameter of methane (4.14×10^{-9} m)

and the viscosities of gas and water phases (1.001×10^{-5} Pa·s and 1.2053 Pa·s, respectively) are consistent with the values reported in the literature [31,32].

② Fractal Theory and Permeability Models: Parameters related to pore structure, such as the fractal dimension (D_f) and tortuosity, are based on fractal theory, which effectively characterizes the complex geometry of pore networks in tight sandstone. These parameters are calculated using equations derived from fractal geometry [23,24].

③ Stress Sensitivity and Initiation Pressure Gradient: The stress sensitivity coefficients (Φ_s and k_s) and initiation pressure gradients (0.005 MPa/m for water and 0.0002 MPa/m for gas) are selected based on stress experiments on tight reservoirs and the specific characteristics of fluid flow in nano- and micro-scale pores [20]. These parameters are critical for accurately representing the non-Darcy flow behavior observed in tight reservoirs.

④ Slip Effects: The slip coefficients ($A_1 = 4/3$ and $A_2 = 1/4$) are taken from well-established slip models applicable to gas flow in nano- and micropores [29]. These coefficients are crucial for modeling enhanced gas flow due to slip effects at low pressures.

⑤ Capillary Forces and Water Film Thickness: The influence of capillary forces and water film thickness is incorporated using experimentally measured values of water film thickness (1 to 20 nm) and critical capillary radius, which are crucial for understanding fluid flow in hydrophilic nanopores [27].

The relevant calculation parameters are shown in Table 1.

Table 1. Calculation parameter information.

Parameter	Symbol	Unit	Value
Boltzmann constant	k_b	J/K	$1.3806505 \times 10^{-23}$
Molecular diameter of methane	d	m	4.14×10^{-9}
Experimental temperature	T	K	400.15
Experimental pressure	P_{ave}	MPa	0.16
First-order slip coefficient	A_1	Dimensionless	1.33
Second-order slip coefficient	A_2	Dimensionless	0.25
Characteristic length of water molecule	λ_w	m	1.50×10^{-9}
Gas viscosity at standard conditions	μ_{gi}	Pa·s	1.001×10^{-5}
Bulk water viscosity	μ_{w1}	Pa·s	1.2053
High-viscosity-region water viscosity	μ_{w2}	Pa·s	3.8547
Universal gas constant	R	J/(mol.K)	8.314462
Molar mass of methane	M	Kg/mol	1.6×10^{-2}
Absolute temperature	T	K	298.15
Rarefied gas effect fitting constant	χ_1	Dimensionless	4
Universal slip coefficient	c	Dimensionless	-1
Rarefied gas effect coefficient at $Kn \rightarrow \infty$	χ_0	Dimensionless	1.19
Critical temperature of methane	T_c	K	190.6
Critical pressure of methane	P_c	MPa	4.6
Real gas effect fitting constant	A_1	Dimensionless	7.9
Real gas effect fitting constant	A_2	Dimensionless	9.00×10^{-6}
Real gas effect fitting constant	A_3	Dimensionless	0.28
Porosity stress sensitivity coefficient	Φ_s	Dimensionless	0.01
Permeability stress sensitivity coefficient	k_s	Dimensionless	0.855
Water-phase starting pressure gradient	g_w	MPa/m	0.005
Gas-phase starting pressure gradient	g_g	MPa/m	0.0002
Atmospheric pressure	P_i	MPa	0.1

The relative permeability model for micron-sized pores established in this study is validated by comparing the relative permeability curves obtained from the model with gas–water relative permeability results obtained from existing studies in the literature, derived through experiments and simulations, as shown in Figure 5.

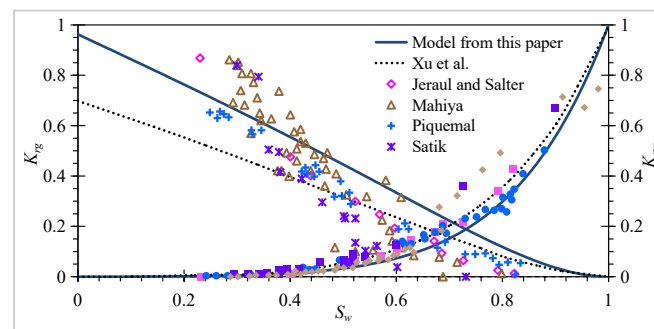


Figure 5. Comparison of gas–water relative permeability curves for micropore models with experimental results and other analytical models.

Jerauld and Salter [33] tested the relative permeability of Berea sandstone, which has a porosity of 0.24 and a high hydrophilic quartz content of 80%. We found that our model’s results align closely with their experimental data, especially at low water saturations. This improved fit is due to our consideration of gas slippage effects and stress sensitivity, which were not accounted for in their model.

Piquemal [34] used a direct method to process experimental data and obtain gas–water relative permeability. Similarly, our model validates well against Piquemal’s experimental data [34], demonstrating the robustness of our approach in capturing the intricate gas–water flow dynamics in tight sandstone.

Satik [35] and Mahiyya [36] employed a steady-state method combined with an X-ray CT scanner to obtain relative permeability curves for steam and liquid water. Their experiments were conducted on Berea sandstone cores, with a maximum experimental pressure of 27 psi. Our model shows a strong correlation with the results from Satik [34] and Mahiyya [36], particularly in capturing the steam–water flow characteristics, due to our comprehensive consideration of gas slippage and stress sensitivity.

Xu et al. [25] established an analytical model for assessing gas–water relative permeability in conventional porous media using fractal theory, but their model did not consider gas slippage, water film, and multi-layer adsorption effects. As shown in Figure 5, the model established in this paper closely matches experimental data from different references and provides a better fit than the model by Xu et al. [25]. This is primarily because their model did not account for gas slippage effects, resulting in significant errors at low water saturation levels.

This comparative analysis indicates that the micron-sized pore relative permeability model constructed in this paper aligns well with experimental data, especially at low water saturation levels. Compared to Xu et al.’s model [25], this study considers more influencing factors, resulting in more accurate predictions of gas-phase relative permeability.

Yassin et al. [37] measured the gas relative permeability curves for a tight gas reservoir with a porosity of 0.043. Using a centrifuge, they desaturated initially fully water-saturated samples to achieve different water saturations. The samples were then subjected to 2000 psi confining pressure and 1000 psi pore pressure at room temperature, and gas relative permeability at different saturations was obtained using a pulse decay permeameter. Multiple tests were conducted to determine the gas relative permeability at various water saturations. The irreducible water saturation S_{w0} was assumed to be the immobile part of the rock framework, and normalized water saturation $S_{wn} = (S_w - S_{w0}) / (1 - S_{w0})$ was used for processing and validation. The gas-phase relative permeability curve obtained from the nanometer-scale pore relative permeability model established in this study was compared with Yassin et al.’s [37] results, as shown in Figure 6. The results calculated using Equation (45) show relatively good agreement with the experimental results.

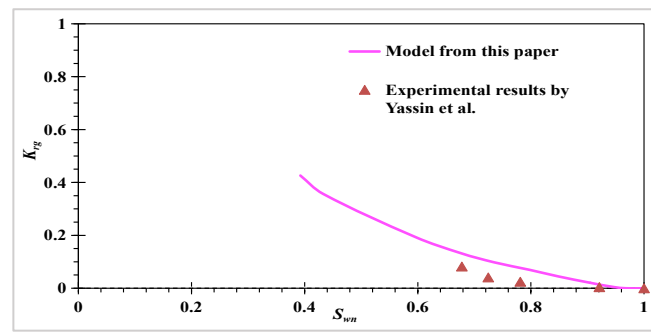


Figure 6. Comparison of gas relative permeability for nanopore model with experimental results (normalized) [37].

The validation above indicates that the model proposed in this paper can reasonably describe the complex gas–water two-phase flow characteristics in tight gas reservoirs with micro-scale and nano-scale pores. However, due to the limited experimental validation points for nanopores, the model’s reliability will be further studied as experimental conditions are optimized in future research.

The key differences and advantages of our model include the incorporation of gas slippage effects and stress sensitivity, the integration of fractal theory, and a comprehensive approach that includes initiation pressure gradients, water film mechanisms, and pore tortuosity. These considerations result in more accurate predictions of gas-phase relative permeability and better alignment with experimental data.

4. Tight Gas Reservoir Productivity Study

The use of massive hydraulic fracturing techniques near horizontal wells to create a complex fracture network can improve the fluid flow properties in the vicinity of the wellbore, making it an effective method for enhancing the development of tight gas reservoirs.

4.1. Physical Modeling and Assumptions for Fractured Horizontal Wells

For tight gas reservoirs that have undergone hydraulic fracturing in horizontal wells, the reservoir structure is divided into three parts: main fractures, fracture networks, and the matrix. In response to the characteristics of reservoir structures formed after massive hydraulic fracturing in horizontal wells, this study proposes a composite flow model aimed at accurately predicting and analyzing the productivity of tight gas reservoirs. This model fully considers the complex fracture network structure formed around horizontal wells through massive fracturing.

Establishing a composite flow model for low-permeability tight gas reservoirs requires subdividing the area. One-quarter of the control area of a single fracture is taken as the research object and divided into three main regions: the main fracture area (Region I), the fractured network stimulated area (Region II), and the unstimulated area (Region III) (see Figure 7).

① Fracture Area (Region I): Fluid flows linearly along the fracture into the horizontal well.

② Fracture Network Stimulated Area (Region II): Serving as a dual-porosity medium superimposed with matrix and fracture networks, fractures are unevenly distributed along the horizontal direction, with their density decreasing with distance. Fluid mainly flows into the main fracture along the y -axis direction.

③ Unstimulated Area (Region III): The outer periphery of the reservoir, where fluid converges through the tips of fractures into the main fracture, exhibiting non-Darcy flow.

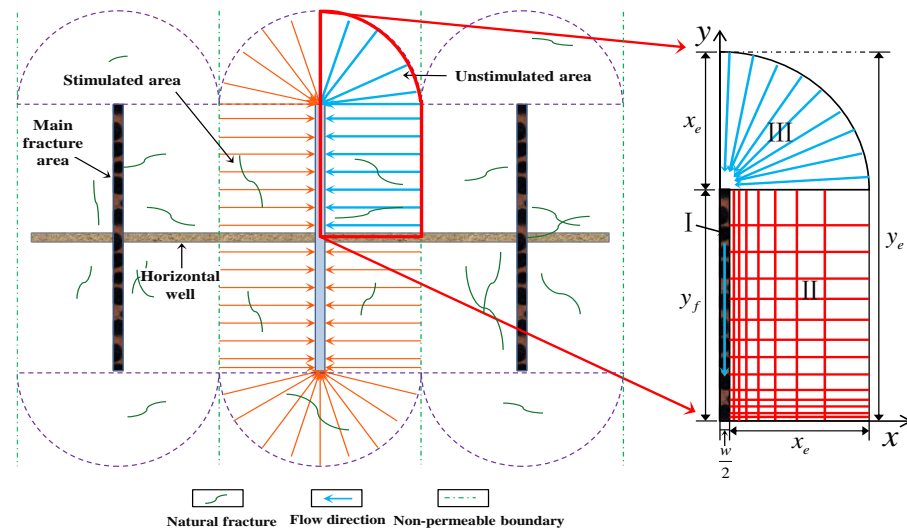


Figure 7. Composite seepage model of non-uniform fracture network structure in fractured horizontal wells. (The red arrow points to an enlarged view of the localized 1/4 area.)

The model is applicable for evaluating the productivity of water-bearing tight gas reservoirs, which often develop micro- and nanopores of different scales. In tight gas reservoirs with high water saturation, gas and water coexist in the pores without mass transfer between them. The model assumptions are as follows:

- ① The reservoir is horizontally distributed, homogeneous, and of uniform thickness;
- ② The fluid within the reservoir and fractures is assumed to be single-phase fluid, isothermal, and under a steady-state flow, with gravity and capillary forces being neglected;
- ③ The water phase in the gas reservoir can flow continuously, exhibiting gas–water two-phase flow, without considering miscible flow;
- ④ Region II is considered a complex reservoir with a fractal dimension D , representing the complex distribution of the fracture network in Euclidean space;
- ⑤ The pressure loss along the horizontal wellbore is assumed to be negligible; the model will consider the pressure sensitivity of fractures and the effect of the initiation pressure gradient;
- ⑥ The artificial fractures are perpendicular to the horizontal wellbore, and all fracture lengths are equal;
- ⑦ The horizontal well produces flow at a fixed bottom-hole pressure, with the horizontal segment located in the center of the reservoir: gas flows from the unmodified boundary area into the fracture network area, and then from the fracture network area into the main fracture.

Limitations and Assumptions of This Study

However, to simplify the model and computations, several assumptions have been made, which inherently introduce certain limitations.

- ① We assume that the reservoir is horizontally distributed, homogeneous, and of uniform thickness. This assumption might not fully reflect the actual heterogeneity of the reservoir, which can significantly affect fluid flow dynamics. Variations in rock properties and pore structures are not accounted for, potentially leading to discrepancies between the model predictions and actual field performance.
- ② The fluid within the reservoir and fractures is considered to be single-phase fluid, isothermal, and under a steady-state flow, with gravity and capillary forces being neglected. In reality, temperature variations and transient flow conditions can influence fluid properties and behavior. Neglecting gravity and capillary forces may oversimplify the flow dynamics, particularly in regions where capillary pressure effects are substantial.

③ The model assumes continuous gas–water two-phase flow without considering miscible flow. This simplification might overlook the interactions between gas and water phases, which can impact relative permeability and flow behavior. The complexity of the fracture network is modeled using a fractal dimension representing its complexity in Euclidean space. While this captures some aspects of fracture complexity, it might not fully represent the actual heterogeneity and connectivity of natural fracture networks.

④ The pressure sensitivity of fractures and the effect of the initiation pressure gradient are considered, but with the assumption that these gradients are constant. This may not reflect real field conditions, where initiation pressure gradients can vary with reservoir pressure and fluid properties. The artificial fractures are assumed to be perpendicular to the horizontal wellbore and of equal length. In practice, variations in hydraulic fractures can significantly influence flow patterns and productivity, which our model may not fully capture.

4.2. Productivity Model of Tight Gas Reservoirs

4.2.1. Constraint Conditions

When gas and water flow in the pores, they form a specific interface shape, such as a crescent shape. The pressure difference between the two sides of the interface is the capillary force, expressed as follows:

$$p_c = p_{0g} - p_{0w} \quad (46)$$

4.2.2. Gas Productivity Model

(1) Region III

Regarding gas and water flowing together, an apparent permeability model has previously been established for the unstimulated zone, considering slip effects (Knudsen diffusion), stress sensitivity (the effect of effective stress on permeability), and the mechanism of water presence at the micrometer–nanometer scale. Therefore, the average apparent permeability of gas in the matrix pores in the unreformed boundary zone can be obtained [38]:

$$\overline{k_{3g}} = \frac{\Phi_e}{\tau} \frac{(R_S - h_{\delta w})^2}{8} (1 + \alpha Kn) \left(1 + \frac{4Kn}{1 + Kn} \right) \quad (47)$$

The relationship between absolute permeability and pore radius can be expressed as follows [39]:

$$K(P) = \frac{\phi(P)R_s^2}{8\tau} \quad (48)$$

Since it is a gas–water two-phase flow, introducing relative permeability gives

$$\overline{k_{3g}} = k_{1g}k_{1rg} \frac{(R_S - h_{\delta w})^2}{R_s^2} (1 + \alpha Kn) \left(1 + \frac{4Kn}{1 + Kn} \right) \quad (49)$$

In the previous sections, relative permeability models for gas in micropores and nanopores were established. To integrate nanopores and micropores and reasonably characterize the overall relative permeability, the concept of nanopore percentage is introduced. Let the nanopore percentage be denoted by χ ; then, the micropore percentage is χ . Combining the relative permeability equations for gas in different pore sizes (Equations (45) and (25)) gives

$$k_{1rg} = \chi k_{rg-nm} + (1 - \chi)k_{rg-\mu m} \quad (50)$$

where k_{rg-nm} is the nano-scale gas relative permeability, which can be obtained from Equation (45); $k_{rg-\mu m}$ is the nano-scale gas relative permeability, which can be obtained

using Equation (25). Combining Equations (49) and (50), the permeability of the gas phase in the unstimulated area is obtained as follows:

$$\overline{k}_{3g} = k_{1g} [\chi k_{rg-nm} + (1 - \chi) k_{rg-\mu m}] \frac{(R_S - h_{\delta w})^2}{R_S^2} (1 + \alpha Kn) \left(1 + \frac{4Kn}{1 + Kn}\right) \quad (51)$$

For the two-phase flow of gas and water, the gas-phase pressure in Region III can be expressed as

$$m_{3g} = m_{0g} + \frac{m_i - m_{0g}}{\ln(2x_e/w)} \ln \frac{2r}{w} \quad (52)$$

The corresponding gas productivity in Region III is

$$q_{3g} = \frac{\pi \overline{k}_{3g} T_{sc} h [m_i - m_{0g} - G^*(x_e - w/2)]}{p_{sc} T \ln(2x_e/w)} \quad (53)$$

Simplifying the pseudo-pressure in Region III gives

$$m_{3g} = 2 \int_{p_w}^{p_{3g}} \frac{p_{3g}}{\mu_g Z} dp_{3g} \approx \frac{p_{3g}^2 - p_w^2}{\mu_g Z} \quad (54)$$

Substituting Equation (55) into Equation (54), we obtain

$$q_{3g} = \pi \overline{k}_{3g} T_{sc} h \left[\frac{p_i^2 - p_{0g}^2}{\mu_g Z} - \frac{p_{0g} G_g}{\mu_g Z} \left(x_e - \frac{w}{2}\right) \right] / \left[p_{sc} T \ln \left(\frac{2x_e}{w}\right) \right] \quad (55)$$

If we assume that $\Omega_{3g} = \frac{p_{sc} T \ln(2x_e/w)}{\pi \overline{k}_{3g} T_{sc} h}$, then $q_{3g} = \left(\frac{p_i^2 - p_{0g}^2}{\mu_g Z} - \frac{p_{0g} G_g}{\mu_g Z} \left(x_e - \frac{w}{2}\right) \right) / \Omega_{3g}$.

(2) Region II

Fractal theory is also introduced to describe the complexity of the fracture network. Therefore, the corrected gas permeability in the fracture network stimulated area is

$$\overline{k}_{2g} = k_{2rg} \left(\frac{x}{w/2}\right)^{D-2-\theta} \left(a S_w k_{2g} e^{\alpha(m_i - \overline{m}_{2g})} + b \right) \left(1 + \frac{3\pi c}{16k_{2g}} \frac{\mu_g D_p}{\overline{m}_{2g}}\right) \left(1 + \frac{d}{\overline{m}_{2g}}\right) \quad (56)$$

For the two-phase flow of gas and water, the expression for gas-phase pressure in Region II based on the mathematical model can be obtained as

$$m_{2g} = m_i + \frac{m_i - (m_w + m_{0g})/2}{x_e^{3+\theta-D} - (w/2)^{3+\theta-D}} \left(x^{3+\theta-D} - x_e^{3+\theta-D}\right) \quad (57)$$

The corresponding Region II gas productivity expression is

$$q_{2g} = \frac{\overline{k}_{2g} T_{sc} y_f h (3 + \theta - D) [m_i - (m_w + m_{0g})/2]}{2 p_{sc} T \frac{w}{2} \left[\left(\frac{x_e}{w/2}\right)^{3+\theta-D} - 1 \right]} \quad (58)$$

Simplifying the pseudo-pressure for Region II gives

$$m_{2g} = 2 \int_{p_w}^{p_{2g}} \frac{p_{2g}}{\mu_g Z} dp_{2g} \approx \frac{p_{2g}^2 - p_w^2}{\mu_g Z} \quad (59)$$

Substituting Equation (59) into Equation (58), we obtain

$$q_{2g} = \frac{\bar{k}_{2g} T_{sc} y_f h}{2 p_{sc} T} \left\{ (3 + \theta - D) \left(\frac{p_i^2 - p_w^2}{\mu_g \bar{Z}} - \frac{1}{2} \left(\frac{p_w^2 + p_{0g}^2}{\mu_g \bar{Z}} \right) \right) \right\} / \left\{ \frac{w}{2} \left[\left(\frac{x_e}{w/2} \right)^{3+\theta-D} - 1 \right] \right\} \quad (60)$$

If we assume that $\Omega_{2g} = \frac{w}{2} \left[\left(\frac{x_e}{w/2} \right)^{3+\theta-D} - 1 \right] \frac{2p_{sc}T}{\bar{k}_{2g}T_{sc}y_f h(3+\theta-D)}$, then

$$q_{2g} = \left(\frac{p_i^2 - p_w^2}{\mu_g \bar{Z}} - \frac{1}{2} \left(\frac{p_w^2 + p_{0g}^2}{\mu_g \bar{Z}} \right) \right) / \Omega_{2g}.$$

(3) Region I

The relative permeability of the gas phase will affect productivity, and the water saturation will also affect the stress sensitivity. Therefore, the permeability of the gas phase in the main fracture zone needs to be corrected:

$$\bar{k}_{1g} = k_{1rg} \left(a S_w k_{1g} e^{\alpha(m_i - \bar{m}_{1g})} + b \right) \left(1 + \frac{3\pi c}{16k_{1g}} \frac{\mu_g D_p}{\bar{m}_{1g}} \right) \left(1 + \frac{d}{\bar{m}_{1g}} \right) \quad (61)$$

where k_{1rg} is the relative permeability of the gas phase in the main fracture area, dimensionless. For gas–water two-phase flow, the seepage mathematical model is

$$\begin{cases} \frac{\partial^2 m_{1g}}{\partial y^2} = 0 \\ m_{1g}|_{y=y_f} = m_{0g}, m_{1g}|_{y=0} = m_w \end{cases} \quad (62)$$

The pressure expression for the gas at the end of the main fracture is

$$m_{1g} = m_w + \frac{m_{0g} - m_w}{y_f} y \quad (63)$$

The gas productivity for Region I is

$$q_{1g} = T_{sc} \bar{k}_{1g} w h (m_{0g} - m_w) / 4 p_{sc} T y_f \quad (64)$$

Simplifying the pseudo-pressure for Region I gives

$$m_{1g} = 2 \int_{p_w}^{p_{1g}} \frac{p_{1g}}{\mu_g \bar{Z}} dp_{1g} \approx \frac{p_{1g}^2 - p_w^2}{\mu_g \bar{Z}} \quad (65)$$

Substituting Equation (65) into Equation (64), we obtain

$$q_{1g} = \frac{T_{sc} \bar{k}_{1g} w h (p_{0g}^2 - p_w^2)}{4 p_{sc} T y_f \mu_g \bar{Z}} \quad (66)$$

If we assume that $\Omega_{1g} = 4 p_{sc} T y_f / (T_{sc} \bar{k}_{1g} w h)$, then $q_{1g} = (p_{0g}^2 - p_w^2) / \Omega_{1g}$.

4.2.3. Gas Productivity of Multi-Stage Fracturing Horizontal Well

In the hydraulic fracturing horizontal well model of tight gas reservoirs, the flow in the main fracture includes two parts: Region III and Region II. Therefore, the gas flow rate formula is

$$q_{1g} = q_{2g} + q_{3g} \quad (67)$$

Substituting each region's gas productivity into Equation (67), we obtain

$$\frac{\left(\frac{p_i^2 - p_{0g}^2}{\mu_g \bar{Z}} - \frac{p_{0g} G_g}{\mu_g \bar{Z}} \left(x_e - \frac{w}{2} \right) \right)}{\Omega_{3g}} + \frac{\left(\frac{p_i^2 - p_w^2}{\mu_g \bar{Z}} - \frac{1}{2} \left(\frac{p_w^2 + p_{0g}^2}{\mu_g \bar{Z}} \right) \right)}{\Omega_{2g}} = \frac{p_{0g}^2 - p_w^2}{\Omega_{1g}} \quad (68)$$

The pressure expression for the gas at the end of the main fracture is

$$p_{0g} = \frac{1}{2A} \left[-B \left(x_e - \frac{w}{2} \right) + \sqrt{B^2 \left(x_e - \frac{w}{2} \right)^2 - 4AC} \right] \quad (69)$$

where $A = \frac{\bar{\mu}_g Z}{\Omega_{1g}} + \frac{0.5}{\Omega_{2g}} + \frac{1}{\Omega_{3g}}$, $B = \frac{G_g}{\Omega_{3g}}$, $C = - \left(\frac{\bar{\mu}_g Z}{\Omega_{1g}} + \frac{p_i^2 - 1.5p_w^2}{\Omega_{2g}} + \frac{p_i^2}{\Omega_{3g}} \right)$.

The equation for the gas-phase flow rate in Region I can thus be obtained. Since the fluid in Region I eventually converges into the horizontal wellbore, the expression for the gas production of a single fractured horizontal well is

$$q_g = 4q_{1g} = 4 \frac{p_{0g}^2 - p_w^2}{\Omega_1} = \left\{ \frac{1}{A^2} \left[-B \left(x_e - \frac{w}{2} \right) + \sqrt{B^2 \left(x_e - \frac{w}{2} \right)^2 - 4AC} \right]^2 - p_w^2 \right\} / \Omega_1 \quad (70)$$

The distribution of the main fractures in a segmented multi-stage fractured horizontal well is shown in Figure 8. According to their positions in the horizontal wellbore, the main fractures can be divided into end fractures, fractures at the ends of segments, and intra-cluster fractures.

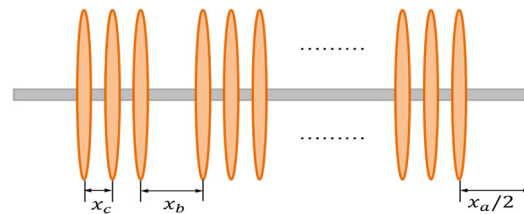


Figure 8. Schematic diagram of fracture placement in a segmented fracturing horizontal well.

Let x_a be the distance between fractures and segment boundary; x_b be the spacing between segments; and x_c be the inter-cluster spacing. Considering the horizontal well is divided into n fracturing segments, each containing m fracturing clusters, the total number of main fractures is $N_F = m \times n$. When calculating the contribution of a single fracture to production, x_e represents half of the spacing between the main fractures. Therefore, the total production of the entire fractured horizontal well can be calculated by replacing the fracture spacing with the appropriate fracture spacing. The formula for this is as follows:

$$Q = n(m-1)q_g(x_c) + (n-1)q_g(x_b) + q_g(x_a) \quad (71)$$

4.2.4. Model Validation and Analysis of Influencing Factors

(1) Case verification

The selected gas reservoir, named gas reservoir A, is a thick sandstone layer formed by braided river channel deposition, with a relatively uniform sand body distribution. The reservoir's initial water saturation is approximately 35%. Two horizontal wells, HW1 and HW2, in gas reservoir A are the focus of this study. These wells are considered low-permeability tight gas wells and are both complete with perforation. HW1 and HW2 have five and six vertical hydraulic fractures, respectively. The boundary pressures of the two wells are 27.1 MPa and 20.1 MPa, respectively. The horizontal wellbore lengths are 510 m and 710 m, respectively. The original permeability of the formation is $K = 0.09$ mD, the half-length of the hydraulic fractures is $L = 100$ m, the fracture width is $w = 0.005$ m, and the radius of the horizontal wellbore is 0.1 m. The thickness of the gas reservoir at HW1 and HW2 is 43 m and 37 m, respectively. The formation temperature is 360K. The stress sensitivity index for both wells is 0.01 MPa^{-1} , and the slip factor is 0.5. In terms of fluid physical properties, the relative density of the gas is 0.78, and the starting pressure gradients of the gas phase and water phase are 0.0006 MPa/m and 0.003 MPa/m , respectively. The viscosities of the gas phase and water phase are $0.04 \text{ mPa}\cdot\text{s}$ and $0.7 \text{ mPa}\cdot\text{s}$, respectively.

Based on the parameters detailed above, the derived equations and programming are applied to calculate the pseudo-pressure, and then the daily gas production of the fractured horizontal well can be obtained. By comparing the calculated daily gas production under different bottom-hole pressure conditions with the actual production data, it is found that (see Table 2) the average errors for the HW1 and HW2 wells are both less than 10%, which indicates that the tight gas reservoir fractured horizontal well productivity model established in this paper is applicable.

Table 2. Comparison between actual production and model-predicted production.

Well Name	Wellbore Pressure (MPa)	Model Prediction ($10^4 \text{ m}^3/\text{d}$)	Measured Data ($10^4 \text{ m}^3/\text{d}$)	Inaccuracies (%)	Average Error (%)
HW1	23.5	3.81	3.45	9.45	8.72
	22.6	4.47	4.12	7.83	
	21.4	5.48	4.93	10.04	
	20.7	6.21	5.74	7.57	
	17	2.57	2.34	8.95	
HW2	16	3.02	2.75	8.94	9.12
	15	3.63	3.32	8.54	
	14	4.18	3.76	10.05	

(2) Analysis of influencing factors

Analyzing the factors affecting the productivity of gas–water two-phase flow in low-permeability fractured horizontal wells based on actual data is important for the development of strategies and for gas field management. Here, the focus is on considering the effects of two-phase flow micro– and nano-scale effects, the water–gas volume ratio, initial water saturation, two-phase flow initiation pressure gradient (G_w and G_g), capillary force, and different drainage capabilities.

In tight gas reservoirs, when considering micro– and nano-scale effects compared to not considering them, the maximum unobstructed flow rate increases by about 2% (see Figure 9). This increase is mainly due to the slip effect in micro– and nano-scale effects, which increases the reservoir’s apparent permeability, leading to an increase in production capacity. The slip effect influences the interaction between gas molecules and pore walls at the micrometer–nanometer scale, reducing the resistance to fluid flow, thereby effectively improving the flow performance and the efficiency of gas production. Additionally, capillary effects and adsorption effects may make gas molecules more prone to flow, reducing flow resistance and increasing gas production capacity. Therefore, in the development of tight gas reservoirs, not considering micro– and nano-scale effects will underestimate the production capacity of tight gas reservoirs.

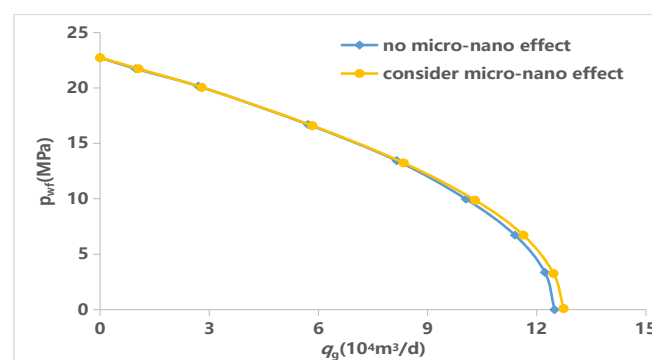


Figure 9. IPR curves of gas wells under the influence of micro– and nano-scale effects.

Figure 10 analyzes the significant impact of initial water saturation on the IPR curve and productivity of gas wells in tight gas reservoirs. As the water saturation increases, the

IPR curve of the gas well shifts to the left, and the production of the gas well decreases. This is mainly because high water saturation reduces the gas saturation that can be produced in the reservoir, while increasing the resistance of gas flow to the wellbore. High water saturation can also lead to water locking, further reducing the production efficiency of the gas well. When water locking occurs, the water in the reservoir hinders the flow of gas, causing an increase in bottom-hole pressure and reducing the effective productivity of the gas well.

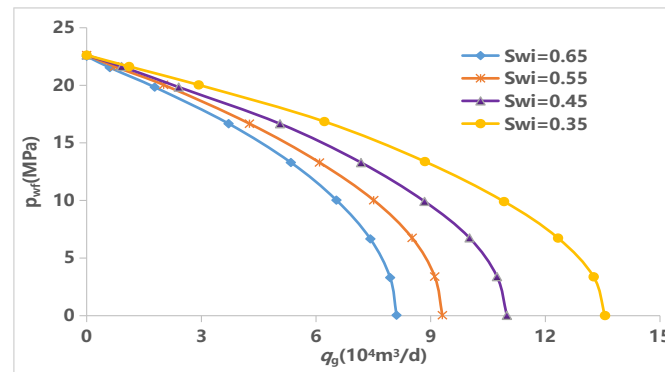


Figure 10. IPR curves of gas wells under different initial water saturations.

Figure 10 illustrates how varying levels of initial water saturation can impact the Inflow Performance Relationship (IPR) curves. Higher initial water saturation leads to a leftward shift of the IPR curve, indicating decreased productivity due to increased water-blocking effects and reduced gas mobility.

Figure 11 shows the impact of the gas and water initiation pressure gradients on the IPR curve in gas–water two-phase flow. As the initiation pressure gradients of the gas and water increase, the IPR curve of the gas well shifts to the left, reducing productivity. In the gas–water two-phase flow of tight gas reservoirs, due to the narrow pore throats, both gas and water phases have initiation pressure gradients. These gradients affect the productivity of the gas well. Lower initiation pressure gradients for both the gas phase and the water phase mean that fluid flow can be achieved with a smaller pressure differential, which is beneficial for improving the gas well’s production.

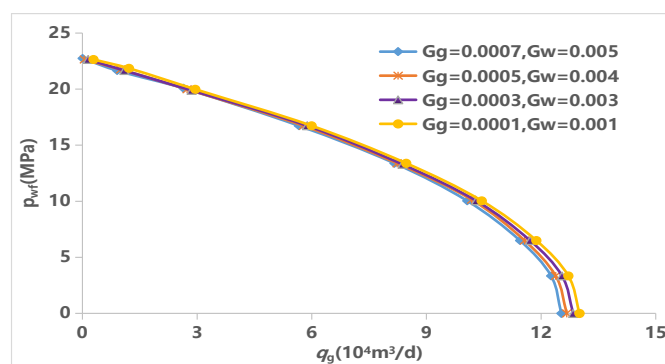


Figure 11. IPR curves of gas wells under different initiation pressure gradients.

Figure 11 shows the influence of gas and water initiation pressure gradients on the IPR curves in gas–water two-phase flow. Higher initiation pressure gradients for both phases cause a leftward shift of the IPR curve, resulting in reduced productivity.

Figure 12 depicts how varying capillary pressures affect gas well productivity. Increased capillary force introduces greater resistance to fluid flow within the pores, reducing gas mobility and causing a leftward shift in the IPR curve, thereby decreasing gas well production capacity.

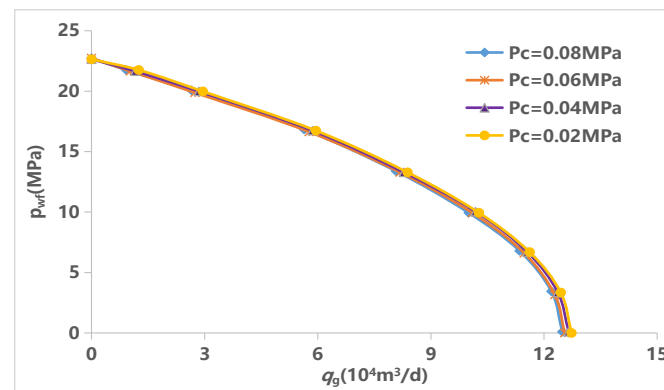


Figure 12. IPR curves of gas wells under different capillary forces.

Figure 13 explores the impact of fracture conductivity on the gas well IPR curve. As the conductivity increases, the IPR curve of the gas well shifts to the right. This shift indicates that at the same reservoir pressure, the gas well can achieve higher production. The reason for this is that higher conductivity reduces the resistance of fluid flow from the reservoir to the wellbore, enhancing fluid mobility and thus improving the production efficiency and output of the gas well.

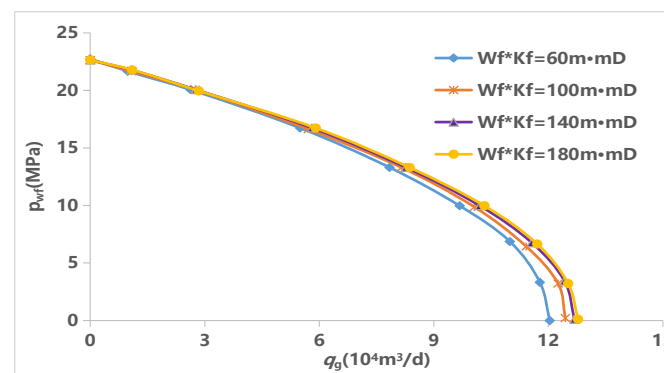


Figure 13. IPR curves of gas wells under different levels of fracture conductivity.

Figure 13 examines the effect of fracture conductivity on the IPR curves. Higher fracture conductivity results in a rightward shift of the IPR curve, indicating enhanced productivity due to improved fluid flow from the reservoir to the wellbore, thus increasing the gas well's production efficiency.

5. Conclusions and Recommendations

This study successfully develops a comprehensive productivity model that incorporates micro- and nano-scale effects for predicting the productivity of water-bearing tight gas reservoirs. The results of this study have significant implications for the oil and gas industry. By incorporating micro- and nano-scale effects, the model more accurately captures the complex gas–water two-phase flow mechanisms in tight gas reservoirs, thereby providing reliable theoretical support and production forecasts crucial for effective reservoir development:

(1) Enhanced Understanding of Flow Mechanisms: By using pore-scale micro-percolation and fractal theory, this study establishes detailed flow rate and relative permeability models for gas–water two-phase flow in micron-scale pores of tight sandstone gas reservoirs. These models incorporate factors such as pore tortuosity, initiation pressure gradients, stress sensitivity, and gas slippage, effectively describing the gas–water flow dynamics in micropores.

(2) Nano-Scale Flow Dynamics: This study also develops flow rate and relative permeability models for gas–water flow in nanopores, considering high-viscosity water films,

gas slippage, stress sensitivity, and initiation pressure gradients. This enhances our understanding of gas–water interactions at the nanometer scale, which is critical for accurately predicting flow behavior in tight sandstone gas reservoirs.

(3) **Three-Region Composite Model:** A sophisticated three-region composite gas–water two-phase flow productivity model is presented, which includes unstimulated areas, fracture network stimulated areas, and main fracture areas. This model integrates the impacts of micro-scale and nano-scale phenomena, such as slippage effects, stress sensitivity, and water saturation, providing a more realistic representation of the reservoir conditions.

(4) **Field Validation and Practical Implications:** The model's predictions are validated against actual production data, demonstrating its reliability. This analysis highlights that neglecting micro- and nano-scale effects can lead to underestimation of reservoir productivity. Incorporating these effects can increase the maximum open flow rate by approximately 2%. Additionally, factors like initial water saturation, initiation pressure gradients for two-phase flow, and capillary forces are found to negatively impact gas well productivity, whereas higher fracture conductivity enhances productivity.

(5) **Optimization of Hydraulic Fracturing:** The developed model aids in optimizing hydraulic fracturing designs, improving development efficiency, and reducing operational costs. By understanding the various factors influencing productivity, engineers can better manage and optimize gas wells, thereby enhancing production performance and extending well life.

(6) **Broader Industrial Application:** This study provides essential technical support for the efficient development and utilization of unconventional natural gas resources, addressing the growing global energy demand and showcasing significant prospects for industrial application.

Temperature variations significantly impact fluid properties such as viscosity and density, thereby affecting flow behavior. Higher temperatures typically decrease fluid viscosity, enhancing flow rates. Although we have assumed isothermal conditions for simplicity in this paper, future work should incorporate a temperature-dependent viscosity model to capture these effects more accurately. Gravity influences fluid distribution, particularly in vertically extensive reservoirs, by affecting capillary pressure and phase segregation. Although our model neglects gravity for simplicity, its inclusion is crucial for accurately predicting fluid flow in such reservoirs. Future model enhancements should consider gravity to address vertical flow dynamics. The diameter of the pipe or pore throats directly influences flow rates according to the Hagen–Poiseuille equation, with smaller diameters resulting in higher resistance and lower flow rates. Our model includes pore diameter as a variable, but a more detailed analysis of pore size distribution could enhance its prediction accuracy. Surface roughness [40] increases frictional resistance, reducing flow rates, and influences gas slippage effects, particularly at the nanometer scale. Our model currently assumes smooth pore walls, simplifying calculations but potentially underestimating flow resistance. Including roughness in future models will provide a more realistic representation of fluid flow in tight gas reservoirs.

These factors—temperature, gravity, pipe diameter, and roughness—play significant roles in determining fluid flow behavior in porous media. While our current model simplifies these effects to focus on other critical mechanisms, we recognize their importance and suggest that future researchers incorporate these parameters in order to improve the accuracy and applicability of predictive models for tight gas reservoirs.

6. Discussion

(1) The Scientific and Industrial Background

The obtained results significantly advance our understanding of gas–water two-phase flow dynamics in tight gas reservoirs. By incorporating micro- and nano-scale effects, including gas slippage, threshold pressure gradients, and stress sensitivity, our model provides a more accurate representation of fluid behavior in unconventional reservoirs.

This scientific advancement is crucial for developing more reliable predictions of reservoir productivity, which has been a persistent challenge in the field of petroleum engineering.

From an industrial perspective, the accurate prediction of gas well productivity is essential for optimizing strategies for the development of tight gas reservoirs. The integration of micro- and nano-scale effects into productivity models enables more precise forecasting, thereby reducing the economic risks associated with drilling and production operations. This is particularly relevant in the context of hydraulic fracturing, where understanding the interplay between fracture networks and fluid flow can lead to more efficient extraction processes, reduced environmental impact, and improved recovery rates.

(2) Other Applications

While our study focuses on the petroleum industry, the methodologies developed could potentially be adapted for use in other industries where fluid dynamics in porous media are critical. For instance, the principles of relative permeability and micro- and nano-scale effects might be applied to enhance the understanding of fluid transport in geothermal reservoirs, in carbon sequestration projects, and even in groundwater hydrology. However, these applications would require further specific research tailored to the unique conditions of each field.

(3) Strengths and Weaknesses

The introduced model excels in integrating micro- and nano-scale effects, such as gas slippage, threshold pressure gradients, and stress sensitivity, which are crucial for accurately predicting fluid flow in tight gas reservoirs. By applying fractal theory to describe complex pore structures and fracture networks, the model effectively simulates real-world conditions, providing a realistic representation of reservoir heterogeneity. Furthermore, the model's validation against actual field data demonstrates its reliability and practical applicability, offering an enhanced understanding of multi-phase flow dynamics and contributing to more accurate productivity predictions.

Despite its strengths, this model relies on several assumptions and simplifications, such as homogeneous reservoir conditions and isothermal fluid flow, which may not fully capture the complexity of all reservoir environments. Additionally, experimental validation for nanopore behaviors is limited, and certain physical phenomena, such as chemical interactions and long-term reservoir compaction effects, are not considered. These limitations may affect the model's accuracy and applicability in more diverse geological formations or over extended periods, highlighting the need for further research and refinement.

7. Workflow Diagram

Step 1. Data Collection and Parameter Selection

① Collect Experimental Data: Gather data from laboratory experiments and field measurements. ② Select Parameters Based on Theoretical Models: Use well-established theoretical models to choose appropriate parameters.

Step 2. Model Formulation

① Develop Flow Rate Models: Create models to calculate the flow rate of fluids in the capillary. ② Develop Relative Permeability Models: Formulate models to determine the relative permeability of gas and water phases.

Step 3. Incorporation of Micro- and Nano-Scale Effects

① Integrate Slip Effects: Consider the slip flow phenomenon in micro- and nanopores. ② Include Initiation Pressure Gradients: Factor in the pressure required to initiate fluid flow in tight gas reservoirs. ③ Consider Stress Sensitivity: Account for the changes in pore structure and permeability caused by stress.

Step 4. Validation

① Validate with Field Data: Compare model predictions with actual field data. ② Compare with Experimental Results: Ensure that model results are consistent with laboratory experiments.

Step 5. Analysis of Influencing Factors

① Analyze Initial Water Saturation: Study the impact of the initial water content in the reservoir on gas productivity. ② Evaluate Capillary Forces: Assess the effect of capillary pressure on fluid flow in the reservoir. ③ Assess Fracture Conductivity: Examine how the ability of fractures to transmit fluids influences overall productivity.

Step 6. Application

① Predict the Productivity of Tight Gas Reservoirs: Use the model to forecast the productivity of reservoirs. ② Optimize Hydraulic Fracturing Designs: Apply insights from the model to enhance fracturing techniques and improve efficiency.

Author Contributions: The research outlined herein benefited from the combined efforts of F.C. and Y.D. in its conceptualization; from the efforts of F.C. in the methodology, software usage, validation (alongside Y.D. and K.W.), formal analysis, investigation, resource gathering, and data management; and from F.C.'s contributions to the original draft, review, and visualization of the manuscript, all under the supervision and project management of Y.D. All authors have read and agreed to the published version of the manuscript.

Funding: This research received no external funding.

Data Availability Statement: Data will be made available on request.

Conflicts of Interest: Author Kun Wang was employed by the company Shenzhen Branch of CNOOC Limited. The remaining authors declare that the research was conducted in the absence of any commercial or financial relationships that could be construed as a potential conflict of interest.

Nomenclature

Symbol	Description	Unit	Symbol	Description	Unit
A_R	Cross-sectional area of the capillary;	m^2	$\Delta P_w/L$	Pressure gradient of the water phase;	Pa/m
ΔP	Pressure difference between the two ends of the capillary;	Pa	d	Euclidean space factor;	Dimensionless
L	Length of the capillary;	m	g_g	Gas-phase initiation pressure gradient;	Pa/m
V	Fluid flow rate in the capillary;	m/s	$\Delta P_g/L$	Pressure gradient in the gas phase;	Pa/m
R	Radial distance from the center of the capillary to any point;	m	K_g	Effective permeability of the gas phase;	mD
R_0	Radius of the capillary;	m	K_w	Effective permeability of the water phase;	mD
μ	Viscosity of the fluid;	Pa·s	A	Cross-sectional area of the characterization unit;	m^3
P	Pressure;	Pa	p_c	Capillary force;	MPa
q_{wmu}	Micropore water-phase velocity;	m/s	p_0	Gas-phase pressure;	MPa
w	Subscripts refer to the water phase;	-	p_0	Water-phase pressure;	MPa
g_w	Initiation pressure gradient of the water phase;	Pa/m	k_{3g}	Apparent permeability of the gas phase in the unstimulated area;	Dimensionless
R_s	Pore diameter at a given pressure when considering stress sensitivity;	m	k_{1rg}	Integrated relative permeability of the gas phase in the unstimulated area;	Dimensionless
P_o	Overlying pressure;	Pa	k_{2rg}	Relative permeability of the gas phase in the stimulated area;	Dimensionless
P_a	Air pressure;	Pa	k_{1rg}	Relative permeability of the gas phase in the main fracture area;	Dimensionless
ϕ_s	Porosity coefficient;	Dimensionless	$L(R)$	Actual length of the pore path;	m
k_s	Permeability coefficient;	Dimensionless	R_0	Pore radius corresponding to the pressure P_o ;	m
V_w	Velocity of the water phase;	m/s	χ_1	Rarefied gas effect fitting constant;	Dimensionless

k_b	Boltzmann constant;	J/K	c	Universal slip coefficient;	Dimensionless
d	Molecular diameter of methane;	m	χ_0	Rarefied gas effect coefficient at $\text{Kn} \rightarrow \infty$;	Dimensionless
T	Experimental temperature;	K	T_c	Critical temperature of methane;	K
P_{ave}	Experimental pressure;	MPa	P_c	Critical pressure of methane;	MPa
A_1	First-order slip coefficient;	Dimensionless	A_1	Real gas effect fitting constant;	Dimensionless
A_2	Second-order slip coefficient;	Dimensionless	A_2	Real gas effect fitting constant;	Dimensionless
λ_w	Characteristic length of a water molecule;	m	A_3	Real gas effect fitting constant;	Dimensionless
μ_{gi}	Gas viscosity under standard conditions;	Pa.s	Φ_s	Porosity stress sensitivity coefficient;	Dimensionless
μ_{w1}	Bulk water viscosity;	Pa.s	k_s	Permeability stress sensitivity coefficient;	Dimensionless
μ_{w2}	High-viscosity-region water viscosity;	Pa.s	g_w	Water-phase starting pressure gradient;	MPa/m
R	Universal gas constant;	J/(mol.K)	g_g	Gas-phase starting pressure gradient;	MPa/m
M	Molar mass of methane.	Kg/mol	P_i	Atmospheric pressure.	MPa

References

- Dai, J.; Ni, Y.; Wu, X. Tight Gas in China and Its Significance in Exploration and Exploitation. *Pet. Explor. Dev.* **2012**, *39*, 277–284. [\[CrossRef\]](#)
- Iii, M.B.A.; Behie, G.A.; Trangenstein, J.A. *Multiphase Flow in Porous Media*. Gulf Pub Co.: Houston, TX, USA, 1981.
- Lei, G.; Dong, P.; Cai, Z.; Zhang, Z.; Dong, R.; Yang, S.; Wu, Z.; Cao, N. Gas-Water Relative Permeability of Tight Sandstone Gas Reservoirs. *Zhongnan Daxue Xuebao (Ziran Kexue Ban)/J. Cent. South Univ. (Sci. Technol.)* **2016**, *47*, 2701–2705.
- Gong, B.; Liu, X.; Qin, G. A Lattice Boltzmann Model for Multi-Component Vapor-Liquid Two Phase Flow. *Pet. Explor. Dev.* **2014**, *41*, 695–702. [\[CrossRef\]](#)
- Li, Y.; Li, X.; Teng, S.; Xu, D. Improved Models to Predict Gas–Water Relative Permeability in Fractures and Porous Media. *J. Nat. Gas. Sci. Eng.* **2014**, *19*, 190–201. [\[CrossRef\]](#)
- Klinkenberge, L.J. The Permeability of Porous Media to Liquids and Gases. *Drill. Prod. Pract.* **1941**, 200–213. [\[CrossRef\]](#)
- Fulton, P.F. The Effect of Gas Slippage on Relative Permeability Measurements. *Prod. Mon.* **1951**, *15*, 14–19.
- Ertekin, T.; King, G.R.; Schwerer, F.C. Dynamic Gas Slippage: A Unique Dual-Mechanism Approach to the Flow of Gas in Tight Formations. *SPE Form. Eval.* **1986**, *1*, 43–52. [\[CrossRef\]](#)
- Shi, J.; Li, X.; Li, Q.; Wang, F.; Sepehrnoori, K. Gas Permeability Model Considering Rock Deformation and Slippage in Low Permeability Water-Bearing Gas Reservoirs. *J. Pet. Sci. Eng.* **2014**, *120*, 61–72. [\[CrossRef\]](#)
- Jiao, K.; Han, D.; Li, J.; Bai, B.; Gong, L.; Yu, B. A Novel LBM-DEM Based Pore-Scale Thermal-Hydro-Mechanical Model for the Fracture Propagation Process. *Comput. Geotech.* **2021**, *139*, 104418. [\[CrossRef\]](#)
- Huang, L.; Jiang, P.; Zhao, X.; Yang, L.; Lin, J.; Guo, X. A Modeling Study of the Productivity of Horizontal Wells in Hydrocarbon-Bearing Reservoirs: Effects of Fracturing Interference. *Geofluids* **2021**, *2021*, 2168622. [\[CrossRef\]](#)
- Yao, J.; Ding, Y.; Sun, H.; Fan, D.; Wang, M.; Jia, C. Productivity Analysis of Fractured Horizontal Wells in Tight Gas Reservoirs Using a Gas–Water Two-Phase Flow Model with Consideration of a Threshold Pressure Gradient. *Energy Fuels* **2023**, *37*, 8190–8198. [\[CrossRef\]](#)
- Wei, B.; Nie, X.; Zhang, Z.; Ding, J.; Shayireatehan, R.; Ning, P.; Deng, D.; Cao, Y. Productivity Equation of Fractured Vertical Well with Gas–Water Co-Production in High-Water-Cut Tight Sandstone Gas Reservoir. *Processes* **2023**, *11*, 3123. [\[CrossRef\]](#)
- Lv, M.; Xue, B.; Guo, W.; Li, J.; Guan, B. Novel Calculation Method to Predict Gas–Water Two-Phase Production for the Fractured Tight-Gas Horizontal Well. *J. Pet. Explor. Prod. Technol.* **2024**, *14*, 255–269. [\[CrossRef\]](#)
- Hu, J.; Zhang, C.; Rui, Z.; Yu, Y.; Chen, Z. Fractured Horizontal Well Productivity Prediction in Tight Oil Reservoirs. *J. Pet. Sci. Eng.* **2017**, *151*, 159–168. [\[CrossRef\]](#)
- Li, J.; Li, X.; Wu, K.; Wang, X.; Shi, J.; Yang, L.; Zhang, H.; Sun, Z.; Wang, R.; Feng, D. Water Sorption and Distribution Characteristics in Clay and Shale: Effect of Surface Force. *Energy Fuels* **2016**, *30*, 8863–8874. [\[CrossRef\]](#)
- Mattia, D.; Calabrò, F. Explaining High Flow Rate of Water in Carbon Nanotubes Via Solid–Liquid Molecular Interactions. *Microfluid. Nanofluid.* **2012**, *13*, 125–130. [\[CrossRef\]](#)
- Myers, T.G. Why Are Slip Lengths so Large in Carbon Nanotubes? *Microfluid. Nanofluid.* **2011**, *10*, 1141–1145. [\[CrossRef\]](#)
- Tocci, G.; Joly, L.; Michaelides, A. Friction of Water on Graphene and Hexagonal Boron Nitride from Ab Initio Methods: Very Different Slippage Despite Very Similar Interface Structures. *Nano Lett.* **2014**, *14*, 6872–6877. [\[CrossRef\]](#) [\[PubMed\]](#)
- Dong, J.-J.; Hsu, J.-Y.; Wu, W.-J.; Shimamoto, T.; Hung, J.-H.; Yeh, E.-C.; Wu, Y.-H.; Sone, H. Stress-Dependence of the Permeability and Porosity of Sandstone and Shale from TCDP Hole-A. *Int. J. Rock. Mech. Min. Sci.* **2010**, *47*, 1141–1157. [\[CrossRef\]](#)
- Katz, A.J.; Thompson, A.H. Fractal Sandstone Pores: Implications for Conductivity and Pore Formation. *Phys. Rev. Lett.* **1985**, *54*, 1325–1328. [\[CrossRef\]](#)

22. Yu, B.; Li, J. Some Fractal Characters of Porous Media. *Fractals* **2001**, *09*, 365–372. [[CrossRef](#)]
23. Yu, B.; Cheng, P. A Fractal Permeability Model for Bi-Dispersed Porous Media. *Int. J. Heat. Mass. Transf.* **2002**, *45*, 2983–2993. [[CrossRef](#)]
24. Bonnet, E.; Bour, O.; Odling, N.E.; Davy, P.; Main, I.; Cowie, P.; Berkowitz, B. Scaling of Fracture Systems in Geological Media. *Rev. Geophys.* **2001**, *39*, 347–383. [[CrossRef](#)]
25. Xu, P.; Yu, B. Developing a New Form of Permeability and Kozeny–Carman Constant for Homogeneous Porous Media by Means of Fractal Geometry. *Adv. Water Resour.* **2008**, *31*, 74–81. [[CrossRef](#)]
26. Burdine, N. Relative Permeability Calculations from Pore Size Distribution Data. *J. Pet. Technol.* **1953**, *5*, 71–78. [[CrossRef](#)]
27. Kim, T.W.; Tokunaga, T.K.; Shuman, D.B.; Sutton, S.R.; Newville, M.; Lanzirotti, A. Thickness Measurements of Nanoscale Brine Films on Silica Surfaces Under Geologic CO₂ Sequestration Conditions Using Synchrotron X-ray Fluorescence. *Water Resour. Res.* **2012**, *48*, 1–13. [[CrossRef](#)]
28. Wu, K.; Chen, Z.; Li, X. Real Gas Transport Through Nanopores of Varying Cross-Section Type and Shape in Shale Gas Reservoirs. *Chem. Eng. J.* **2015**, *281*, 813–825. [[CrossRef](#)]
29. Karniadakis, G.; Beskok, A.; Aluru, N. *Microflows and Nanoflows: Fundamentals and Simulation*; Springer Science & Business Media: Berlin/Heidelberg, Germany, 2006; Volume 29.
30. Cao, B.-Y.; Sun, J.; Chen, M.; Guo, Z.-Y. Molecular Momentum Transport at Fluid-Solid Interfaces in Mems/Nems: A Review. *Int. J. Mol. Sci.* **2009**, *10*, 4638–4706. [[CrossRef](#)]
31. Zhang, T.; Li, X.; Li, J.; Feng, D.; Wu, K.; Shi, J.; Sun, Z.; Han, S. A Fractal Model for Gas–Water Relative Permeability in Inorganic Shale with Nanoscale Pores. *Transp. Porous Med.* **2018**, *122*, 305–331. [[CrossRef](#)]
32. Wu, K.; Chen, Z.; Li, J.; Li, X.; Xu, J.; Dong, X. Wettability Effect on Nanoconfined Water Flow. *Proc. Natl. Acad. Sci. USA* **2017**, *114*, 3358–3363. [[CrossRef](#)]
33. Jerauld, G.R.; Salter, S.J. The Effect of Pore-Structure on Hysteresis in Relative Permeability and Capillary Pressure: Pore-Level Modeling. *Transp. Porous Med.* **1990**, *5*, 103–151. [[CrossRef](#)]
34. Piquemal, J. Saturated Steam Relative Permeabilities of Unconsolidated Porous Media. *Transp. Porous Media* **1994**, *17*, 105–120. [[CrossRef](#)]
35. Satik, C.; Horne, R.N. A Measurement of Steam-Water Relative Permeability. In Proceedings of the 23rd Workshop on Geothermal Reservoir Engineering, Stanford, CA, USA, 26–28 January 1998; Stanford University: Stanford, CA, USA, 1998.
36. Mahiya, G.F. *Experimental Measurement of Steam-Water Relative Permeability*; MS Report; Stanford University: Stanford, CA, USA, 1999.
37. Yassin, M.R.; Dehghanpour, H.; Wood, J.; Lan, Q. A Theory for Relative Permeability of Unconventional Rocks with Dual-Wettability Pore Network. *Spe J.* **2016**, *21*, 1970–1980. [[CrossRef](#)]
38. Sun, Z.; Shi, J.; Wu, K.; Xu, B.; Zhang, T.; Chang, Y.; Li, X. Transport Capacity of Gas Confined in Nanoporous Ultra-Tight Gas Reservoirs with Real Gas Effect and Water Storage Mechanisms Coupling. *Int. J. Heat. Mass. Transf.* **2018**, *126*, 1007–1018. [[CrossRef](#)]
39. Wang, J.; Liu, H.; Wang, L.; Zhang, H.; Luo, H.; Gao, Y. Apparent Permeability for Gas Transport in Nanopores of Organic Shale Reservoirs Including Multiple Effects. *Int. J. Coal Geol.* **2015**, *152*, 50–62. [[CrossRef](#)]
40. Li, J.; Zhang, Y.; Lin, L.; Zhou, Y. Study on the Shear Mechanics of Gas Hydrate-Bearing Sand-Well Interface with Different Roughness and Dissociation. *Bull. Eng. Geol. Environ.* **2023**, *82*, 404. [[CrossRef](#)]

Disclaimer/Publisher’s Note: The statements, opinions and data contained in all publications are solely those of the individual author(s) and contributor(s) and not of MDPI and/or the editor(s). MDPI and/or the editor(s) disclaim responsibility for any injury to people or property resulting from any ideas, methods, instructions or products referred to in the content.